Appl. Comput. Math., Vol.24, No.2, 2025, pp.277-311
DOI: 10.30546/1683-6154.24.2.2025.277

STRUCTURAL AND PRACTICAL PARAMETER IDENTIFICATION OF AN IMMUNO-RESPIRATORY EPIDEMIC MODEL: SENSITIVITY ANALYSIS APPROACH

J.Y. YANG[1,2,*], S. WU[1,2], G.H. DI[3], Z. JIN[1,2]

Abstract. In this investigation, we introduce a sophisticated multi-scale immune-respiratory transmission model that incorporates the intricate nested rule. We analyze the global stability of the equilibria by constructing Lyapunov functions. To comprehensively explore the identifiability of the parameters, we employ the esteemed techniques of principal component analysis and the eigenvalue method, utilizing pristine, noise-free data. We further validate the practical identifiability of these parameters by employing Monte Carlo Simulation and the approximate Bayesian calculation, leveraging the wealth of available dataset. Moreover, the results obtained from our meticulous sensitivity analysis reinforce the identifiability of the parameters, suggesting that curtailing the replication rate and transmission rate of SARS-CoV-2 within hosts plays a pivotal role in attenuating the spread of COVID-19.

Keywords: The Nested Approach, Practical Identifiability, Principal Component Analysis, Eigenvalue Approach.

AMS Subject Classification: 92D30.

1. Introduction

The respiratory infection is an infectious disease that impacts the respiratory system, encompassing both upper and lower respiratory tract infections and including influenza and COVID-19. SARS-CoV-2, also known as severe acute respiratory syndrome coronavirus 2, is the virus responsible for the outbreak of the Corona Virus Disease 2019 (COVID-19). This novel coronavirus has posed great challenges to the international community, as it is a previously unidentified pathogen. As a result, insights into SARS-CoV-2 and the associated pandemic are being steadily enhanced through ongoing research. With the accumulation of data and research, we have made significant strides in comprehending various facets of COVID-19. While some significant progresses have been made in understanding COVID-19 transmission, it is crucial to acknowledge that there persist lacunae in our comprehension because SARS-CoV-2 continues to undergo genetic mutation and a cascade of novel variants incessantly emerge. These mutations can result in substantial alterations to the viruses's amino acid sequences, which can impact their pathological properties. Such modifications may affect the transmissibility of the pathogen by influencing elemental attributes such as the rate of viral replication, the avidity towards host cell receptors, and the pattern of viral excretion [1, 33]. Besides, the existence of genetic variations may influence the efficacy of vaccines, thus necessitating a perpetual pursuit towards refining the immunization process [11]. Vaccination and therapeutic strategies are two main prevention strategies for curbing COVID-19 transmission. However, the implementation of

[1]Complex Systems Research Center, Shanxi University, Taiyuan, 030006, China
[2]Shanxi Key Laboratory of Mathematical Techniques in Complex Systems, Shanxi University, Taiyuan, 030006, China
[3]School of Mathematics and Information Technology, Yuncheng University, Yuncheng, 044000, China
[*]Corresponding author e-mail: yjyang66@sxu.edu.cn
Manuscript received 9 August 2024.

these control measures requires sustained efforts over an extended period until complete disease eradication is accomplished [12]. The emergence of a new virus poses distinctive challenges in terms of studying its behavior and developing effective strategies to combat it [31].

Mathematical modeling assumes a pivotal function in comprehending and foretelling the comportment of infectious diseases. Through harnessing sophisticated mathematical methodologies, many scholars endeavor to fabricate intricate models that encapsulate the multifaceted dynamics of diseases, thus lending valuable supports in crafting efficacious measures for containment. A large proportion of these models are lonely established on an individual basis or at a population level. Actually, an infectious disease can be characterized as a malady caused by a pathogen or its noxious byproduct, originating from the transmission between an infected individual, an infected beast, or a tainted lifeless entity to a vulnerable host. This process refers to pathogenetic kinetics at an individual level and the transmission at population level. Hence, multi-scale modeling emerges as a powerful approach to investigate these complex patterns, incorporating multiple levels of detail and different spatial and temporal scales [17, 20]. Many scholars have employed various methods to build multi-scale COVID-19 models linking within-host and between-host dynamics. One of popular models established by the nested law assumes that the parameters of the between-host model are functions of the within-host variables [36,48,50]. The environmental transmission pathway was incorporated into a fractional-order epidemic model, and investigating the stability of each feasible equilibrium [26]. Another well-known multi-scale COVID-19, called agent based model has been used to estimate various interventions for mitigating the COVID-19 prevalence [7, 27]. Besides, some network models have been used to COVID-19 heterogeneous transmission across differential spatial scales [2,41]. However, the aforementioned results primarily concentrate on the transmission dynamics and parameter estimation of COVID-19 models, while they overlook the identification of model parameters.

Parameter identification involves uniquely determining the parameter values of a model or system, which is crucial for enhancing the reliability and predictive capability of the model. Hence, it is a necessary step before parameter estimation that can optimize the performance of the system. By accurately identifying parameters, we can improve the overall reliability and predictive power of the model, and also provide a solid foundation for informed decision-making. The identifiability of parameters typically relies on the structure of the candidate model, the quality and quantity of the available data, and any constraints that may exist within the parameter space. Numerous existing literatures have focused on the theoretical and numerical methods for assessing parameter identifiability. The structural identifiability of some transmission and therapy parameters has been studied in a tumor model in [19]. In [43], the authors developed a structurally and practically identifiable analysis for a set of Zika virus disease models and they found that the direct transmission rate was practically unidentifiable. In [32], the authors conducted an extensive overview of various methodologies for assessing both structural and practical identifiability of models described by ordinary differential equations (ODEs). The book that is given in [8] delves into the methodology of system identification, exploring various test criteria for its application. To our best knowledge, there are a limited body of researches available that focuses on detecting the parameter identifiability of multi-scale epidemic models. In [44], the authors used the differential algebra to explore the structural identifiability of the within-host model and they adopt the Monte Carlo Simulation method to investigate the practical identifiability of the between-host model.

The novel contributions of this paper are twofold. Firstly, to the best of our knowledge, we initially provide a comprehensive framework for detecting the structural and practical identifiability of a multi-scale model for COVID-19 transmission. The findings of our analysis suggest that the system may be unidentifiable if only a specific set of data or both micro and macro data are available. Secondly, the outcomes of our sensitivity analysis indicate that efforts to inhibit the replication and transmission rates of the SARS-CoV-2 virus within hosts, as well as the

transmission rates among individuals, may represent the most effective strategies for mitigating the spread of COVID-19.

The structure of this paper is organized as follows: The next section focuses on developing a comprehensive exploration of an immuno-COVID-19 model that connects the within-host and between-host dynamics. In Section 3, we employ the least square method to fit the solution to the model by using cumulative cases and SARS-CoV-2 viral loads. We perform parameter identification based on a sensitivity analysis approach and give the identifiable possibility of the multi-scale model parameters in Section 4. We further conduct a practical identifiability analysis using such two data sets in Section 5. In Section 6, we conduct approximate Bayesian calculation on the estimated parameters to derive an approximation of the posterior distribution of the parameters. Section 7 is dedicated to an uncertainty analysis of the coupled model, evaluating how variations in the parameters of interest affect the degree of an infection. We present numerical simulations in Section 8 to examine the impact of several factors on infection dynamics. Finally, in the concluding section, we summarize our findings and offer a brief discussion.

2. Formulation of the model

Let T and T_I on behalf of the quantities of healthy and infected target cells, respectively. Let V stands for the count of the SARS-CoV-2 load in the host. To capture the trade-offs of the within-host dynamic, we utilize the intra-host model proposed in [29] as follows:

$$\begin{aligned}
\frac{\mathrm{dT}(\tau)}{\mathrm{d}\tau} &= \mathrm{d_T}(\mathrm{T}(0)-\mathrm{T}(\tau)) - \rho \mathrm{T}(\tau)\mathrm{V}(\tau),\\
\frac{\mathrm{dT_I}(\tau)}{\mathrm{d}\tau} &= \rho \mathrm{T}(\tau)\mathrm{V}(\tau) - \mathrm{d_{T_I}}\mathrm{T_I}(\tau),\\
\frac{\mathrm{dV}(\tau)}{\mathrm{d}\tau} &= \pi_{\mathrm{V}}\mathrm{T_I}(\tau) - \mathrm{d_V}\mathrm{V}(\tau),
\end{aligned} \tag{1}$$

where $d_T T(0)$ represents the ongoing replication of uninfected epithelial cells and $T(0)$ represents the initial number of uninfected cells. $d_j (j = T, T_I, V)$ represents the death rate of healthy epithelial cells, infected epithelial cells, or the SARS-CoV-2, ρ is the infection rate of the within host, π_V is the production rate of an infected epithelial cell. τ is the age-since infection variable. The system that is given in (1) has initial values as $T(0) = T_0 \geq 0, T_I(0) = T_{I0} \geq 0, V(0) = V_0 \geq 0$. According to the results in [29], we have known that there exists a positive viral equilibrium

$$\mathrm{E^W} = (\mathrm{T}^*, \mathrm{T}_\mathrm{I}^*, \mathrm{V}^*) = \left(\frac{\mathrm{T}(0)}{\mathrm{R_0^W}}, \frac{\mathrm{d_T d_V}}{\rho \pi_{\mathrm{V}}}(\mathrm{R_0^W}-1), \frac{\mathrm{d_T}}{\rho}(\mathrm{R_0^W}-1)\right)$$

of the within-host system (1) with $R_0^W = \frac{\rho \pi_V T(0)}{d_{T_I} d_V} > 1$ and it is asymptotically globally stable.

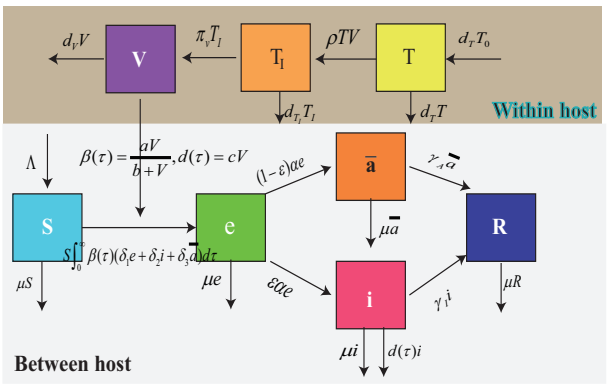


Figure 1. The flowchart of a multi-scale epidemic model (1)-(3).

For the inter-host model, we consider the impact of asymptotic patients on COVID-19 transmission at the population level. That is, people who exhibit no clinical symptoms, such as fever, cough, sore throat, or abnormal chest CT findings, but test positive for COVID-19 etiology in respiratory and other samples. Essentially, they are asymptomatic after the incubation period but test positive for nucleic acid. So in our model, individuals in the latent compartment can either progress to the symptomatic or asymptomatic stage. We categorize the total population into five mutual classes, susceptible (S), pre-symptomatic (e), infectious (i), asymptomatic ($\bar{a}$), and recovered (R). Based on the framework of a nested law (see the flowchart of Fig.1), we construct a multi-scale COVID-19 transmission model as follows:

$$
\begin{aligned}
&\frac{\mathrm{dS(t)}}{\mathrm{dt}} = \Lambda - \delta_1 \mathrm{S(t)} \int_0^\infty \beta(\tau)\mathrm{e}(\tau,\mathrm{t})\mathrm{d}\tau - \delta_2 \mathrm{S(t)} \int_0^\infty \beta(\tau)\mathrm{i}(\tau,\mathrm{t})\mathrm{d}\tau \\
&- \delta_3 \mathrm{S(t)} \int_0^\infty \beta(\tau)\bar{\mathrm{a}}(\tau,\mathrm{t})\mathrm{d}\tau - \mu \mathrm{S(t)}, \\
&\frac{\partial \mathrm{e}(\tau,\mathrm{t})}{\partial \tau} + \frac{\partial \mathrm{e}(\tau,\mathrm{t})}{\partial \mathrm{t}} = -(\alpha(\tau)+\mu)\mathrm{e}(\tau,\mathrm{t}), \\
&\mathrm{e}(0,\mathrm{t}) = \delta_1 \mathrm{S(t)} \int_0^\infty \beta(\tau)\mathrm{e}(\tau,\mathrm{t})\mathrm{d}\tau + \delta_2 \mathrm{S(t)} \int_0^\infty \beta(\tau)\mathrm{i}(\tau,\mathrm{t})\mathrm{d}\tau + \delta_3 \mathrm{S(t)} \int_0^\infty \beta(\tau)\bar{\mathrm{a}}(\tau,\mathrm{t})\mathrm{d}\tau, \\
&\frac{\partial \mathrm{i}(\tau,\mathrm{t})}{\partial \tau} + \frac{\partial \mathrm{i}(\tau,\mathrm{t})}{\partial \mathrm{t}} = -\gamma_{\mathrm{I}}(\tau)\mathrm{i}(\tau,\mathrm{t}) - \mathrm{d}(\tau)\mathrm{i}(\tau,\mathrm{t}) - \mu \mathrm{i}(\tau,\mathrm{t}), \\
&\mathrm{i}(0,\mathrm{t}) = \epsilon \int_0^\infty \alpha(\tau)\mathrm{e}(\tau,\mathrm{t})\mathrm{d}\tau, \\
&\frac{\partial \bar{\mathrm{a}}(\tau,\mathrm{t})}{\partial \tau} + \frac{\partial \bar{\mathrm{a}}(\tau,\mathrm{t})}{\partial \mathrm{t}} = -\gamma_{\mathrm{A}}(\tau)\bar{\mathrm{a}}(\tau,\mathrm{t}) - \mu \bar{\mathrm{a}}(\tau,\mathrm{t}), \\
&\bar{\mathrm{a}}(0,\mathrm{t}) = (1-\epsilon) \int_0^\infty \alpha(\tau)\mathrm{e}(\tau,\mathrm{t})\mathrm{d}\tau, \\
&\frac{\mathrm{dR(t)}}{\mathrm{dt}} = \int_0^\infty \gamma_{\mathrm{I}}(\tau)\mathrm{i}(\tau,\mathrm{t})\mathrm{d}\tau + \int_0^\infty \gamma_{\mathrm{A}}(\tau)\bar{\mathrm{a}}(\tau,\mathrm{t})\mathrm{d}\tau - \mu \mathrm{R(t)}.
\end{aligned}
\tag{2}
$$

The meanings of the parameters of model (3) are detailed in Table 1. The linkage rule across the two scales is established by:

$$
\beta(\tau) = \frac{\mathrm{aV}(\tau)}{\mathrm{b} + \mathrm{V}(\tau)}, \ \mathrm{d}(\tau) = \mathrm{cV}(\tau),
$$

where a and c are scale coefficients and b is the half-saturation coefficient. This suggests that the transmission rate and the death rate due to COVID-19 are directly related to the consistency of SARS-CoV-2 loads, in line with the consequences in [48]. Experimental evidence has shown a correlation between the infection rate and the viral load within the body [22]. Our choice of the joint functions is inspired by the work in [22, 48].

TABLE 1. The meanings of parameters in the model (3).

Parameters	Description
Λ	Population birth rate
μ	Natural death rate
1^{α}	Incubation period
ϵ	Proportion of individuals who transition from latent to symptomatic
γ_I	Recovery rate about symptomatic individual
γ_A	Recovery rate about asymptomatic individual
a	Scale parameter
b	Subsaturation coefficient
c	Scale parameter
δ_1	Probability that a susceptible individual becomes pre-symptomatic person after being infected by a pre-symptomatic individual
δ_2	Probability that a susceptible individual becomes pre-symptomatic person after being infected by a symptomatic individual
δ_3	Probability that a susceptible individual becomes pre-symptomatic person after being infected by a asymptomatic individual

Define $F(t) = \int_0^{\infty} f(\tau, t)d\tau, f = e, i, \bar{a}; F = E, I, A$, we can rewrite system (2) as below

$$\begin{aligned}
\frac{\mathrm{dS(t)}}{\mathrm{dt}} &= \Lambda - \delta_1\beta(\mathrm{V})\mathrm{S(t)E(t)} - \delta_2\beta(\mathrm{V})\mathrm{S(t)I(t)} - \delta_3\beta(\mathrm{V})\mathrm{S(t)A(t)} - \mu\mathrm{S(t)},\\
\frac{\mathrm{dE(t)}}{\mathrm{dt}} &= \delta_1\beta(\mathrm{V})\mathrm{S(t)E(t)} + \delta_2\beta(\mathrm{V})\mathrm{S(t)I(t)} + \delta_3\beta(\mathrm{V})\mathrm{S(t)A(t)} - (\alpha+\mu)\mathrm{E(t)},\\
\frac{\mathrm{dI(t)}}{\mathrm{dt}} &= \epsilon\alpha\mathrm{E(t)} - \gamma_{\mathrm{I}}\mathrm{I(t)} - \mathrm{d(V)I(t)} - \mu\mathrm{I(t)},\\
\frac{\mathrm{dA(t)}}{\mathrm{dt}} &= (1-\epsilon)\alpha\mathrm{E(t)} - \gamma_{\mathrm{A}}\mathrm{A(t)} - \mu\mathrm{A(t)},\\
\frac{\mathrm{dR(t)}}{\mathrm{dt}} &= \gamma_{\mathrm{I}}\mathrm{I(t)} + \gamma_{\mathrm{A}}\mathrm{A(t)} - \mu\mathrm{R(t)}.
\end{aligned} \tag{3}$$

here we have used the fact that $\alpha(\tau) = \alpha, \gamma_{\mathrm{I}}(\tau) = \gamma_{\mathrm{I}}$ and $\gamma_{\mathrm{A}}(\tau) = \gamma_{\mathrm{A}}$ and $\mathrm{V} = \mathrm{d_T}(\mathrm{R_0^W} - 1)/\rho$. System (3) has the following initial conditions

$$\mathrm{S}(0) = \mathrm{S}_0 > 0, \mathrm{E}(0) = \mathrm{E}_0 \geq 0, \mathrm{I}(0) = \mathrm{I}_0 \geq 0, \mathrm{A}(0) = \mathrm{A}_0 \geq 0, \mathrm{R}(0) = \mathrm{R}_0 \geq 0.$$

Model (1) is regarded as a fast subsystem since the interactions within the host, such as the replication, delegation, and production of SARS-CoV-2, occur on relatively short time scales, ranging from hours to days. In contrast, model (3) is taken as a slow subsystem because the transmission and spread of COVID-19 between hosts occur on longer time scales, extending from weeks to months or even years. Factors within model (3) like contact patterns, human behaviors, and public health interventions profoundly influence the overall transmission patterns of a COVID-19 outbreak in a community or population.

First, the multi-scale model (1)-(3) has a disease-free equilibrium solutions (DFEs), denoted by $\boldsymbol{\varepsilon}^0 = (T^*, T_I^*, V^*, S^0, E^0, I^0, A^0, R^0) = (T^*, T_I^*, V^*, \frac{\Lambda}{\mu}, 0, 0, 0, 0)$. Drawing from the discussions on the basic reproduction number in [13, 47], we can define the new infection matrix $\mathscr{F}$ and transition matrix $\mathscr{V}$ by:

$$\mathscr{F} = \begin{pmatrix} \delta_1\beta(V^*)S^0 & \delta_2\beta(V^*)S^0 & \delta_3\beta(V^*)S^0 \\ 0 & 0 & 0 \\ 0 & 0 & 0 \end{pmatrix}, \mathscr{V} = \begin{pmatrix} \alpha+\mu & 0 & 0 \\ -\epsilon\alpha & \gamma_I + d(V^*) + \mu & 0 \\ -(1-\epsilon)\alpha & 0 & \gamma_A + \mu \end{pmatrix}.$$

Certainly, the basic reproduction number R_0^B is the spectral radius of the matrix $\mathscr{F}\mathscr{V}^{-1}$, i.e.,

$$\mathrm{R_0^B} = \rho(\mathscr{F}\mathscr{V}^{-1}) = \mathrm{R_{0E}} + \mathrm{R_{0I}} + \mathrm{R_{0A}},$$

where

$$\mathrm{R_{0E}} = \frac{\delta_1\beta(\mathrm{V^*})\mathrm{S^0}}{\alpha+\mu},\ \mathrm{R_{0I}} = \frac{\epsilon\alpha\delta_2\beta(\mathrm{V^*})\mathrm{S^0}}{(\alpha+\mu)(\gamma_\mathrm{I}+\mathrm{d(V^*)}+\mu)},$$
$$\mathrm{R_{0A}} = \frac{(1-\epsilon)\alpha\delta_3\beta(\mathrm{V^*})\mathrm{S^0}}{(\alpha+\mu)(\gamma_\mathrm{A}+\mu)}.$$

The decomposition of R_0^B into three components, where R_{0E} (resp. R_{0I}, R_{0A}) is the contribution of latency (resp. infection, asymptomatic) to host-to-host transmission. Particularly, R_{0E} represents the average number of secondary cases $\delta_1\beta(V^*)$ produced by one latent patient during its latent period $\frac{1}{\alpha+\mu}$; R_{0I} is the mean number of secondary cases $\delta_2\beta(V^*)S^0$ produced by one symptomatic patient during its infectious period $\frac{1}{\gamma_I+d(V^*)+\mu}$ surviving at the probability $\frac{\alpha}{\alpha+\mu}$ and become an symptomatic sicker at the proportion of ϵ. R_{0A} is the mean number of secondary cases $\delta_3\beta(V^*)S^0$ produced by one asymptomatic patient during its infectious period $\frac{1}{\gamma_A+\mu}$ surviving at the probability $\frac{\alpha}{\alpha+\mu}$ and becoming an asymptotic patient at the proportion of $1-\epsilon$.

Now, we are in a position on the global stability of between host system (3). To achieve this goal, let us define the following set:

$$\Omega := \{(\mathrm{S_0}, \mathrm{E_0}, \mathrm{I_0}, \mathrm{A_0}, \mathrm{R_0}) \in \mathbb{R}_+^5 : \mathrm{S_0} + \mathrm{E_0} + \mathrm{I_0} + \mathrm{A_0} + \mathrm{R_0} \le \mathrm{S^0}\}$$

and it is not hard to see that Ω is a positively invariant set of system (3).

Theorem 1. *If $R_0^B \le 1 < R_0^W$, the disease-free equilibrium $\boldsymbol{\varepsilon}^0$ of between host system (3) is globally asymptotically stable for each $(S_0, E_0, I_0, A_0, R_0) \in \Omega$.*

Proof. For each $(S_0, E_0, I_0, A_0, R_0) \in \Omega$, let us pick up a candidate Lyapunov function by as:

$$\mathrm{L^V(t)} = \mathrm{S(t)} - \mathrm{S^0} - \mathrm{S^0}\ln\frac{\mathrm{S(t)}}{\mathrm{S^0}} + \mathrm{a_1E(t)} + \mathrm{a_2I(t)} + \mathrm{a_3A(t)},$$

where a_1, a_2, a_3 are positive coefficients and they will be determined later. Now, we take the derivative of L^V along the solution of system (3) to derive

$$\begin{aligned}
\frac{\mathrm{dL^V}}{\mathrm{dt}}\Big|_{(3)} =& \left(1-\frac{\mathrm{S^0}}{\mathrm{S}}\right)\frac{\mathrm{dS}}{\mathrm{dt}} + \mathrm{a_1}\frac{\mathrm{dE}}{\mathrm{dt}} + \mathrm{a_2}\frac{\mathrm{dI}}{\mathrm{dt}} + \mathrm{a_3}\frac{\mathrm{dA}}{\mathrm{dt}}\\
=&(1-\frac{\mathrm{S^0}}{\mathrm{S}})\frac{\mathrm{dS}}{\mathrm{dt}} + \mathrm{a_1}\frac{\mathrm{dE}}{\mathrm{dt}} + \mathrm{a_2}\frac{\mathrm{dI}}{\mathrm{dt}} + \mathrm{a_3}\frac{\mathrm{dA}}{\mathrm{dt}}\\
=&(1-\frac{\mathrm{S^0}}{\mathrm{S}})\left(\mu\mathrm{S^0}(1-\frac{\mathrm{S}}{\mathrm{S^0}}) - \delta_1\beta(\mathrm{V^*})\mathrm{SE} - \delta_2\beta(\mathrm{V^*})\mathrm{SI} - \delta_3\beta(\mathrm{V^*})\mathrm{SA}\right)\\
&+ \mathrm{a_1}\left(\delta_1\beta(\mathrm{V^*})\mathrm{SE} + \delta_2\beta(\mathrm{V^*})\mathrm{SI} + \delta_3\beta(\mathrm{V^*})\mathrm{SA} - (\alpha+\mu)\mathrm{E}\right)\\
&+ \mathrm{a_2}\left(\epsilon\alpha\mathrm{E} - (\gamma_\mathrm{I}+\mathrm{d(V^*)}+\mu)\mathrm{I}\right)\\
&+ \mathrm{a_3}\left((1-\epsilon)\alpha\mathrm{E} + (\gamma_\mathrm{A}+\mu)\mathrm{A}\right)\\
=&\mu\mathrm{S^0}(1-\frac{\mathrm{S}}{\mathrm{S^0}})(1-\frac{\mathrm{S^0}}{\mathrm{S}}) + (\mathrm{a_1}-1)\delta_1\beta(\mathrm{V^*})\mathrm{SE} + (\mathrm{a_1}-1)\delta_2\beta(\mathrm{V^*})\mathrm{SI} + (\mathrm{a_1}-1)\delta_3\beta(\mathrm{V^*})\mathrm{SA}\\
&+ (\alpha+\mu)\left(\frac{\delta_1\beta(\mathrm{V^*})\mathrm{S^0}}{\alpha+\mu} - \mathrm{a_1} + \mathrm{a_2}\frac{\epsilon\alpha}{\alpha+\mu} + \mathrm{a_3}\frac{(1-\epsilon)\alpha}{\alpha+\mu}\right)\mathrm{E}\\
&+ (\gamma_\mathrm{I}+\mathrm{d(V^*)}+\mu)\left(\frac{\delta_2\beta(\mathrm{V^*})\mathrm{S^0}}{\gamma_\mathrm{I}+\mathrm{d(V^*)}+\mu} - \mathrm{a_2}\right)\mathrm{I}\\
&+ (\gamma_\mathrm{A}+\mu)\left(\frac{\delta_3\beta(\mathrm{V^*})\mathrm{S^0}}{\gamma_\mathrm{A}+\mu} - \mathrm{a_3}\right)\mathrm{A}.
\end{aligned}$$

Set $a_1 = 1, a_2 = \frac{\delta_2\beta(V^*)S^0}{\gamma_I + d(V^*) + \mu}, a_3 = \frac{\delta_3\beta(V^*)S^0}{\gamma_A + \mu}$, then the formula simplifies to

$$\frac{\mathrm{dL^V}}{\mathrm{dt}} = \mu \mathrm{S^0}(1 - \frac{\mathrm{S}}{\mathrm{S^0}})(1 - \frac{\mathrm{S^0}}{\mathrm{S}}) + (\alpha + \mu)\left(\mathrm{R_0^B} - 1\right)\mathrm{E}.$$

If $R_0^B < 1$, then $\dot{L^V}(t) \leq 0$. If $\frac{dL^V}{dt} = 0$, then $S(t) = S^0$ and $E(t) = 0$ for $t \in \mathbb{R}_+$. This suggests that the largest invariant set of $\{(S_0, E_0, I_0, A_0, R_0) \in \Omega | \dot{L^V}(t) = 0\} = \{\boldsymbol{\varepsilon}^0\}$. According to LaSalle's Invariance Principle, $\boldsymbol{\varepsilon}^0$ is globally asymptotically stable in Ω if $R_0^B < 1 < R_0^W$.

Additionally, if $R_0^B = 1$, then

$$\frac{\mathrm{dL^V}}{\mathrm{dt}} = \mu \mathrm{S^0}(1 - \frac{\mathrm{S}}{\mathrm{S^0}})(1 - \frac{\mathrm{S^0}}{\mathrm{S}}) \leq 0. \tag{4}$$

The equality of (4) holds if and only if $S(t) = S^0$ for each $t \in \mathbb{R}_+$. From the first equation of (3), we have that $\delta_1\beta(V^*)S^0E(t) + \delta_2\beta(V^*)S^0I(t) + \delta_3\beta(V^*)S^0A(t) = 0$. The nonnegativity of parameters ensures that $E(t) = I(t) = A(t) = 0$. We use LaSalle's invariance principle again to obtain the global stability of $\boldsymbol{\varepsilon}^0$. □

Theorem 2. *If* $\min\{R_0^W, R_0^B\} > 1$, *system* (3) *has an endemic equilibrium point* $\boldsymbol{\varepsilon}^* = (S^*, E^*, I^*, A^*, R^*)$ *and it is globally asymptotically stable for every* $(S_0, E_0, I_0, A_0, R_0) \in \Omega \setminus \{\boldsymbol{\varepsilon}^0\}$, *where*

$$\mathrm{S^*} = \frac{\Lambda}{\mu \mathrm{R_0^B}}, \quad \mathrm{E^*} = \frac{\Lambda}{\mu + \alpha}\left(1 - \frac{1}{\mathrm{R_0^B}}\right), \quad \mathrm{I^*} = \frac{\epsilon\alpha \mathrm{E^*}}{\gamma_\mathrm{I} + \mathrm{d(V^*)} + \mu},$$
$$\mathrm{A^*} = \frac{(1-\epsilon)\alpha \mathrm{E^*}}{\gamma_\mathrm{A} + \mu}, \quad \mathrm{R^*} = \frac{\epsilon\alpha\gamma_\mathrm{I}\mathrm{E^*}}{\mu(\gamma_\mathrm{I} + \mathrm{d(V^*)} + \mu)} + \frac{(1-\epsilon)\alpha\gamma_\mathrm{A}\mathrm{E^*}}{\mu(\gamma_\mathrm{A} + \mu)}.$$

Proof. The existence is a straightforward consequence for solving a set of algebra equations of letting the left sides of the derivatives of system (3) be 0. Now, we are concerned with the global stability of $\boldsymbol{\varepsilon}^*$. Let us choose the following Lyapunov function

$$\mathrm{L_f(t)} = \mathrm{L_1^f(t)} + \frac{\delta_2\beta(\mathrm{V^*})\mathrm{S^*I^*}}{\epsilon\alpha\mathrm{E^*}}\mathrm{L_2^f(t)} + \frac{\delta_3\beta(\mathrm{V^*})\mathrm{S^*A^*}}{(1-\epsilon)\alpha\mathrm{E^*}}\mathrm{L_3^f(t)}$$

with

$$\mathrm{L_1^f} = \left(\mathrm{S} - \mathrm{S^*} - \mathrm{S^*}\ln\frac{\mathrm{S}}{\mathrm{S^*}}\right) + \left(\mathrm{E} - \mathrm{E^*} - \mathrm{E^*}\ln\frac{\mathrm{E}}{\mathrm{E^*}}\right),$$
$$\mathrm{L_2^f} = \left(\mathrm{I} - \mathrm{I^*} - \mathrm{I^*}\ln\frac{\mathrm{I}}{\mathrm{I^*}}\right),\ \mathrm{L_3^f} = \left(\mathrm{A} - \mathrm{A^*} - \mathrm{A^*}\ln\frac{\mathrm{A}}{\mathrm{A^*}}\right).$$

First, differentiating L_1^f of equations (2) and using the relationship of components of the endemic equilibrium lead to

$$\begin{aligned}
\frac{\mathrm{dL_1^f}}{\mathrm{dt}}\Big|_{(3)} &= \left(1 - \frac{\mathrm{S^*}}{\mathrm{S}}\right)\frac{\mathrm{dS}}{\mathrm{dt}} + \left(1 - \frac{\mathrm{E^*}}{\mathrm{E}}\right)\frac{\mathrm{dE}}{\mathrm{dt}} \\
&= \left(1 - \frac{\mathrm{S^*}}{\mathrm{S}}\right)(\Lambda - \delta_1\beta(\mathrm{V^*})\mathrm{SE} - \delta_2\beta(\mathrm{V^*})\mathrm{SI} - \delta_3\beta(\mathrm{V^*})\mathrm{SA} - \mu\mathrm{S}) \\
&\quad + \left(1 - \frac{\mathrm{E^*}}{\mathrm{E}}\right)(\delta_1\beta(\mathrm{V^*})\mathrm{SE} + \delta_2\beta(\mathrm{V^*})\mathrm{SI} + \delta_3\beta(\mathrm{V^*})\mathrm{SA} - (\alpha + \mu)\mathrm{E}) \\
&= \left(1 - \frac{\mathrm{S^*}}{\mathrm{S}}\right)\left(\delta_1\beta(\mathrm{V^*})\mathrm{S^*E^*}\left(1 - \frac{\mathrm{SE}}{\mathrm{S^*E^*}}\right) + \delta_2\beta(\mathrm{V^*})\mathrm{S^*I^*}\left(1 - \frac{\mathrm{SI}}{\mathrm{S^*I^*}}\right)\right. \\
&\quad \left. + \delta_3\beta(\mathrm{V^*})\mathrm{S^*A^*}\left(1 - \frac{\mathrm{SA}}{\mathrm{S^*A^*}}\right)\right) + \left(1 - \frac{\mathrm{E^*}}{\mathrm{E}}\right)\left(\delta_1\beta(\mathrm{V^*})\mathrm{ES^*}\left(\frac{\mathrm{S}}{\mathrm{S^*}} - 1\right)\right. \\
&\quad \left. + \delta_2\beta(\mathrm{V^*})\mathrm{S^*I^*}\left(\frac{\mathrm{SI}}{\mathrm{S^*I^*}} - \frac{\mathrm{E}}{\mathrm{E^*}}\right) + \delta_3\beta(\mathrm{V^*})\mathrm{S^*A^*}\left(\frac{\mathrm{SA}}{\mathrm{S^*A^*}} - \frac{\mathrm{E}}{\mathrm{E^*}}\right)\right)
\end{aligned}$$

$$
\begin{aligned}
=&\delta_1\beta(\mathrm{V}^*)\mathrm{S}^*\mathrm{E}^*\left(2-\frac{\mathrm{S}^*}{\mathrm{S}}-\frac{\mathrm{S}}{\mathrm{S}^*}\right)+\mu\mathrm{S}^*\left(2-\frac{\mathrm{S}^*}{\mathrm{S}}-\frac{\mathrm{S}}{\mathrm{S}^*}\right)\\
&+\delta_2\beta(\mathrm{V}^*)\mathrm{S}^*\mathrm{I}^*\left(-\left(1-\frac{\mathrm{S}^*}{\mathrm{S}}\right)\left(\frac{\mathrm{SI}}{\mathrm{S}^*\mathrm{I}^*}-1\right)+\left(1-\frac{\mathrm{E}^*}{\mathrm{E}}\right)\left(\frac{\mathrm{SI}}{\mathrm{S}^*\mathrm{I}^*}-\frac{\mathrm{E}}{\mathrm{E}^*}\right)\right)\\
&+\delta_3\beta(\mathrm{V}^*)\mathrm{S}^*\mathrm{A}^*\left(-\left(1-\frac{\mathrm{S}^*}{\mathrm{S}}\right)\left(\frac{\mathrm{SA}}{\mathrm{S}^*\mathrm{A}^*}-1\right)+\left(1-\frac{\mathrm{E}^*}{\mathrm{E}}\right)\left(\frac{\mathrm{SA}}{\mathrm{S}^*\mathrm{A}^*}-\frac{\mathrm{E}}{\mathrm{E}^*}\right)\right)\\
=&\delta_1\beta(\mathrm{V}^*)\mathrm{S}^*\mathrm{E}^*\left(2-\frac{\mathrm{S}^*}{\mathrm{S}}-\frac{\mathrm{S}}{\mathrm{S}^*}\right)+\mu\mathrm{S}^*\left(2-\frac{\mathrm{S}^*}{\mathrm{S}}-\frac{\mathrm{S}}{\mathrm{S}^*}\right)\\
&+\delta_2\beta(\mathrm{V}^*)\mathrm{S}^*\mathrm{I}^*\left(2-\frac{\mathrm{S}^*}{\mathrm{S}}-\frac{\mathrm{E}}{\mathrm{E}^*}+\frac{\mathrm{I}}{\mathrm{I}^*}-\frac{\mathrm{SIE}^*}{\mathrm{S}^*\mathrm{I}^*\mathrm{E}}\right)\\
&+\delta_3\beta(\mathrm{V}^*)\mathrm{S}^*\mathrm{A}^*\left(2-\frac{\mathrm{S}^*}{\mathrm{S}}-\frac{\mathrm{E}}{\mathrm{E}^*}+\frac{\mathrm{A}}{\mathrm{A}^*}-\frac{\mathrm{SAE}^*}{\mathrm{S}^*\mathrm{A}^*\mathrm{E}}\right)\\
\leq&\delta_2\beta(\mathrm{V}^*)\mathrm{S}^*\mathrm{I}^*\left(\frac{\mathrm{I}}{\mathrm{I}^*}-\ln\frac{\mathrm{I}}{\mathrm{I}^*}+\ln\frac{\mathrm{E}}{\mathrm{E}^*}-\frac{\mathrm{E}}{\mathrm{E}^*}\right)\\
&+\delta_3\beta(\mathrm{V}^*)\mathrm{S}^*\mathrm{A}^*\left(\frac{\mathrm{A}}{\mathrm{A}^*}-\ln\frac{\mathrm{A}}{\mathrm{A}^*}+\ln\frac{\mathrm{E}}{\mathrm{E}^*}-\frac{\mathrm{E}}{\mathrm{E}^*}\right).
\end{aligned}
$$

Second, we calculate the derivative of L_2^f along the trajectory of system (3) to obtain

$$
\begin{aligned}
\frac{\mathrm{dL_2^f}}{\mathrm{dt}}=&\left(1-\frac{\mathrm{I}^*}{\mathrm{I}}\right)\frac{\mathrm{dI}}{\mathrm{dt}}=\left(1-\frac{\mathrm{I}^*}{\mathrm{I}}\right)(\epsilon\alpha\mathrm{E}-(\gamma_\mathrm{I}+\mathrm{d}(\mathrm{V}^*)+\mu)\mathrm{I}(\mathrm{t}))\\
=&\left(1-\frac{\mathrm{I}^*}{\mathrm{I}}\right)\left(\epsilon\alpha\mathrm{E}^*\left(\frac{\mathrm{E}}{\mathrm{E}^*}-\frac{\mathrm{I}}{\mathrm{I}^*}\right)\right)\\
=&\epsilon\alpha\mathrm{E}^*\left(1+\frac{\mathrm{E}}{\mathrm{E}^*}-\frac{\mathrm{I}}{\mathrm{I}^*}-\frac{\mathrm{EI}^*}{\mathrm{E}^*\mathrm{I}}\right)\\
\leq&\epsilon\alpha\mathrm{E}^*\left(\frac{\mathrm{E}}{\mathrm{E}^*}-\ln\frac{\mathrm{E}}{\mathrm{E}^*}+\ln\frac{\mathrm{I}}{\mathrm{I}^*}-\frac{\mathrm{I}}{\mathrm{I}^*}\right).
\end{aligned}
$$

Third, we compute the derivative of L_3^f along the solution of system (3) to get

$$
\begin{aligned}
\frac{\mathrm{dL_3^f}}{\mathrm{dt}}=&\left(1-\frac{\mathrm{A}^*}{\mathrm{A}}\right)\frac{\mathrm{dA}}{\mathrm{dt}}=\left(1-\frac{\mathrm{A}^*}{\mathrm{A}}\right)((1-\epsilon)\alpha\mathrm{E}-(\gamma_\mathrm{A}+\mu)\mathrm{A})\\
=&\left(1-\frac{\mathrm{A}^*}{\mathrm{A}}\right)\left((1-\epsilon)\alpha\mathrm{E}^*\left(\frac{\mathrm{E}}{\mathrm{E}^*}-\frac{\mathrm{A}}{\mathrm{A}^*}\right)\right)\\
=&(1-\epsilon)\alpha\mathrm{E}^*\left(1+\frac{\mathrm{E}}{\mathrm{E}^*}-\frac{\mathrm{A}}{\mathrm{A}^*}-\frac{\mathrm{EA}^*}{\mathrm{E}^*\mathrm{A}}\right)\\
\leq&(1-\epsilon)\alpha\mathrm{E}^*\left(\frac{\mathrm{E}}{\mathrm{E}^*}-\ln\frac{\mathrm{E}}{\mathrm{E}^*}+\ln\frac{\mathrm{A}}{\mathrm{A}^*}-\frac{\mathrm{A}}{\mathrm{A}^*}\right).
\end{aligned}
$$

In these cases, we have used the inequality $1-x\leq-\ln x$ to acquire the following inequalities

$$
\begin{aligned}
2-\frac{\mathrm{S}^*}{\mathrm{S}}-\frac{\mathrm{E}}{\mathrm{E}^*}+\frac{\mathrm{I}}{\mathrm{I}^*}-\frac{\mathrm{SIE}^*}{\mathrm{S}^*\mathrm{I}^*\mathrm{E}}\leq&-\ln\frac{\mathrm{S}^*}{\mathrm{S}}-\frac{\mathrm{E}}{\mathrm{E}^*}+\frac{\mathrm{I}}{\mathrm{I}^*}-\ln\frac{\mathrm{SIE}^*}{\mathrm{S}^*\mathrm{I}^*\mathrm{E}}\\
=&\frac{\mathrm{I}}{\mathrm{I}^*}-\ln\frac{\mathrm{I}}{\mathrm{I}^*}+\ln\frac{\mathrm{E}}{\mathrm{E}^*}-\frac{\mathrm{E}}{\mathrm{E}^*},\\
1+\frac{\mathrm{E}}{\mathrm{E}^*}-\frac{\mathrm{I}}{\mathrm{I}^*}-\frac{\mathrm{EI}^*}{\mathrm{E}^*\mathrm{I}}\leq&\frac{\mathrm{E}}{\mathrm{E}^*}-\frac{\mathrm{I}}{\mathrm{I}^*}-\ln\frac{\mathrm{EI}^*}{\mathrm{E}^*\mathrm{I}}\\
=&\frac{\mathrm{E}}{\mathrm{E}^*}-\ln\frac{\mathrm{E}}{\mathrm{E}^*}+\ln\frac{\mathrm{I}}{\mathrm{I}^*}-\frac{\mathrm{I}}{\mathrm{I}^*},
\end{aligned}
$$

$$\begin{aligned}1+\frac{\mathrm{E}}{\mathrm{E}^*}-\frac{\mathrm{A}}{\mathrm{A}^*}-\frac{\mathrm{EA}^*}{\mathrm{E}^*\mathrm{A}} \leq & \frac{\mathrm{E}}{\mathrm{E}^*}-\frac{\mathrm{A}}{\mathrm{A}^*}-\ln\frac{\mathrm{EA}^*}{\mathrm{E}^*\mathrm{A}} \\ = & \frac{\mathrm{E}}{\mathrm{E}^*}-\ln\frac{\mathrm{E}}{\mathrm{E}^*}+\ln\frac{\mathrm{A}}{\mathrm{A}^*}-\frac{\mathrm{A}}{\mathrm{A}^*}.\end{aligned}$$

Hence,

$$\frac{\mathrm{dL}^{\mathrm{f}}}{\mathrm{dt}}\Big|_{(3)}=\frac{\mathrm{dL}_1^{\mathrm{f}}}{\mathrm{dt}}+\frac{\delta_2\beta(\mathrm{V}^*)\mathrm{S}^*\mathrm{I}^*}{\epsilon\alpha\mathrm{E}^*}\frac{\mathrm{dL}_2^{\mathrm{f}}}{\mathrm{dt}}+\frac{\delta_3\beta(\mathrm{V}^*)\mathrm{S}^*\mathrm{A}^*}{(1-\epsilon)\alpha\mathrm{E}^*}\frac{\mathrm{dL}_3^{\mathrm{f}}}{\mathrm{dt}}\leq 0.$$

Moreover, we have noticed that the equality of $\frac{dL^f}{dt}=0$ holds if and only if $(S,E,I,A,R)=(S^*,E^*,I^*,A^*,R^*)$. According to LaSalle's Invariance Principle, the endemic equilibrium point $\boldsymbol{\varepsilon}^*$ is globally asymptotically stable in the set $\Omega\setminus\{\boldsymbol{\varepsilon}^0\}$ as long as $\min\{R_0^W,R_0^B\}>1$. □

As aforementioned before, parameter identifiability is a crucial prerequisite for making reliable predictions and designing effective controls in statistical and mathematical models. When model parameters are unidentifiable, it can result in an ill-posed inverse problem for parameter estimation, leading to estimates that provide misleading insights or predictions. The main objective of this paper is to assess the structural and practical identifiability of parameters in the coupled multi-scale model (1)-(3), ensuring that parameter estimation is accurate. However, the traditional approaches for dealing with structural identifiability, such as differential algebra, the implicit function theorem, and direct test method, are not applicable due to the complexity and the high dimensionality of model (1)-(3). Consequently, we must explore an effective method to surmount this challenge and provide a satisfactory determination of the structural identifiability. In [19], a sensitivity analysis method was introduced to present an identifiable rank of model parameters with observable data. In what follows, we will adopt this method to detect the parameter identifiability of model (1)-(3).

3. Estimation of the parameter

We have recognized that the immuno-COVID-19 model (1) and (3) collectively involve 18 distinct parameters and 8 initial values. In order to facilitate parameter identifiability, we prefer to assign fixed values to certain parameters, thereby increasing the likelihood of successful identification.

(1) We set the value of natural mortality to $\mu=3\times10^{-5}$ day^{-1} [21, 48]. According to the reported data from USA Census Bureau [46] and the total population in America in 2020, as cited in [5] $N=3.3$ million, we have calculated the birth rate to be $\Lambda=9897$ day^{-1}.
(2) The experimental data from [29] indicates that the death rate of healthy epithelial cells is $d_T=0.001$ day^{-1}, the death rate of unhealthy epithelial cells is $d_{T_I}=0.11$ day^{-1}, and the delegation rate of the SARS-CoV-2 is $d_V=5.36$ day^{-1}, respectively.
(3) The incubation period of COVID-19 varies from a span of 2 to 18 days [15]. Furthermore, individuals afflicted with the unaltered variant of SARS-CoV-2, showcasing mild or asymptomatic symptoms, generally attain convalescence within a fortnight [6], prompting us to assign a value of $\alpha=1/14$ day^{-1}.
(4) The infectious period of asymptomatic patient is approximately 7 days [34] and thus we set $\gamma_A=1/7$ day^{-1}.
(5) According to the results in [38], among the 712 individuals embarked on the Diamond Princess, who indisputably tested positive for the perilous SARS-CoV-2, a staggering total of 410 displayed no overt symptoms of this disease. Ergo, we ascertain the ratio of these individuals who experienced the absence of symptoms to be an impressive 58%. Consequently, we shall assign the variable ϵ as one-half (1/2) in our subsequent analyses.

Our goal is to provide accurate and reliable parameter estimation and anticipation using the available data. We have collected the cumulative COVID-19 case data for the USA from March 4 to April 25, 2020 [45], as well as the average viral load data for COVID-19 patients over a 21-day period [52]. Both datasets are based on the original strain of the virus. According to the model and data from [29, 45, 52], we have chosen the initial conditions for the model as $T(0) = 25, T_I(0) = 2.59, V(0) = 153, S(0) = 3000000, E(0) = 2500, I(0) = 83, A(0) = 1000, R(0) = 0$. Actually, we need to identify the remaining parameters of the model (1) and (3), which include $\rho, \pi_V, \delta_1, \delta_2, \delta_3, \gamma_I, a, b, c$.

For the identifiability of the parameter set $\Theta = \{\rho, \pi_V, \delta_1, \delta_2, \delta_3, \gamma_I, a, b, c\}$, we adjust the parameters to fit the solution curve closely to the real data. The goal is to minimize the sum of the distances between the model's predicted values and the actual data points. Consequently, we define the following objective function:

$$\mathrm{J}(\Theta) = \min_{\theta} \sum |\mathrm{y_j}(\mathrm{t_i}) - \mathrm{Y_j^i}|^2 \ (\mathrm{j} = 1, \mathrm{i} = 53 \text{ or } \mathrm{j} = 2, \mathrm{i} = 21), \tag{5}$$

with solely known the cumulative COVID-19 cases and viral load data. Besides, $y_j(t)(j = 1, 2)$ satisfies the following equations:

$$\frac{\mathrm{dy_1(t)}}{\mathrm{dt}} = \epsilon\alpha \mathrm{E(t)}, \text{ and } \mathrm{y_2(t)} = \mathrm{V(t)}.$$

Then, given the availability of two distinct data sets, we would select a candidate objective function that is tailored to fit both datasets simultaneously:

$$\mathrm{J}(\Theta) = \min_{\theta} \left(\frac{1}{53} \sum_{\mathrm{m}=1}^{53} \frac{|\mathrm{y_1(t_m)} - \mathrm{Y_1^m}|^2}{\hat{\mathrm{Y}}_1^2} + \frac{1}{21} \sum_{\mathrm{n}=1}^{21} \frac{|\mathrm{y_2(t_n)} - \mathrm{Y_2^n}|^2}{\hat{\mathrm{Y}}_2^2} \right). \tag{6}$$

In the objective functions (5) and (6), Y_j^i represent the cumulative COVID-19 cases or viral load data at discrete time points t_i, respectively, while $y_j(t_i)$ denote the solution curves of the model at time t_i. The symbols $\hat{Y}_1$ and $\hat{\mathrm{Y}}_2$ represent the average cumulative COVID-19 cases and the average SARS-CoV-2 load across all time points, respectively:

$$\hat{\mathrm{Y}}_1 = \frac{1}{53} \sum_{\mathrm{m}=1}^{53} \mathrm{Y_1^m} \ , \ \hat{\mathrm{Y}}_2 = \frac{1}{21} \sum_{\mathrm{n}=1}^{21} \mathrm{Y_2^n}.$$

We conduct the least squares method to optimize functions (5) and (6) for the estimated parameters, as shown in Table 2. Fig.2 displays the fitting outcomes using two separate groups of independent data, while Fig.3 depicts the fitting results when using both data sets simultaneously.

TABLE 2. Parameter estimation results of coupled system.

	Cumulative Cases	Viral Load	Simultaneous	
Parameters	Value	Value	Value	Unites
ρ	0.32	3.17×10^{-4}	8.06×10^{-4}	day^{-1}
π_V	9.72	249.33	133.80	day^{-1}
δ_1	0.46	0.49	0.63	-
δ_2	0.49	0.10	0.25	-
δ_3	0.79	0.60	0.44	-
γ_I	0.09	0.08	0.08	day^{-1}
a	2.15×10^{-7}	2.12	1.45×10^{-7}	-
b	2.58	46.24	14.35	-
c	0.96	7.95	25.48	-

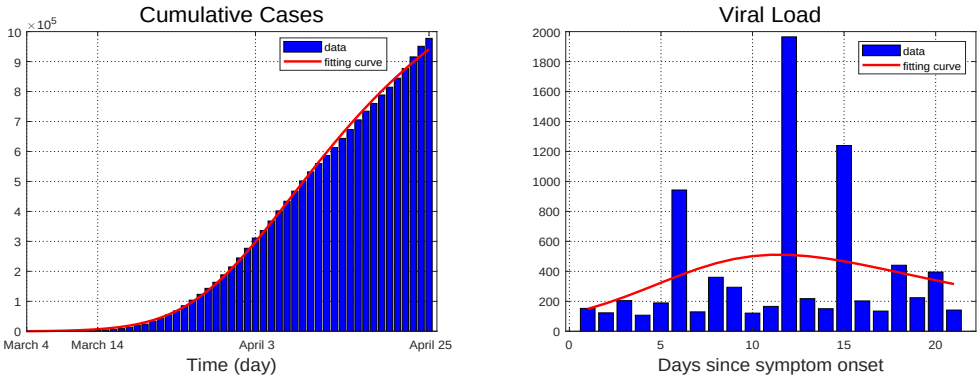


FIGURE 2. The cumulative cases data and viral load data (blue bars) fit the associated solutions (red curves) of the multi-scale model, respectively, with the estimated values presented in columns 2 and 3 of Table 2.

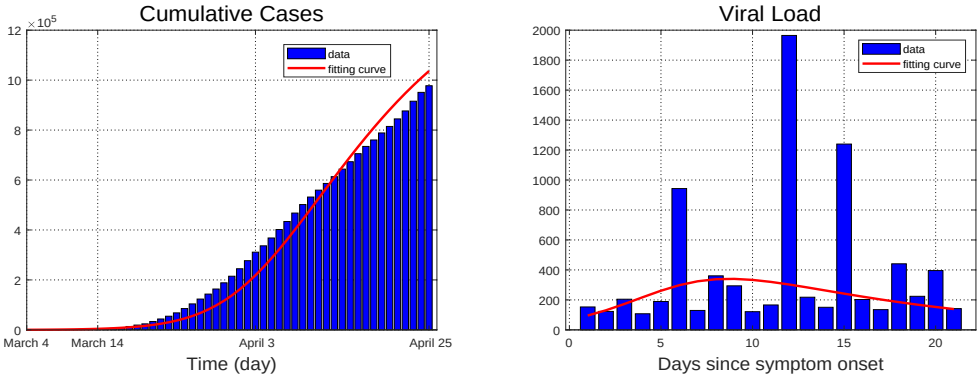


FIGURE 3. The fitting snapshots with both cumulative COVID-19 cases and SARS-CoV-2 loads (blue bars), the red curves relevant the associated solutions to multi-scale model (1) and (3).

4. Parameter identifiability based on sensitivity analysis

Sensitivity-based identifiability analysis encompasses the assessment of the model outputs' responsiveness towards variations in input parameters. If a subtle alteration in a parameter engenders a momentous change in the model's output, which implies that the parameter's potential for identifiability. In contrast, when modifications in a parameter exert negligible influence on the model output, its identifiability may be jeopardized. Indubitably, the sensitivity analysis methodology conventionally entails assessing the responsiveness of a model at a specific nominal parameter value. This nominal value acts as a pivotal reference point, around which the identifiability analysis is orchestrated. By appraising the sensitivity matrix composed of derivatives of the model's outputs with respect to the parameters at that nominal values, one can attain profound insights into the identifiability of all parameters. First, we need to introduce an identifiable concept proposed in [28, 37].

Definition 1. Globally at-a-point identifiable: At the fixed point θ^* in the parameter space Θ, the system can uniquely determine the parameter vector. If two different parameter vectors $\theta, \theta^* \in \Theta$ lead to the same system output $\mathrm{y}(\mathrm{u}, \theta) = \mathrm{y}(\mathrm{u}, \theta^*)$ for any admissible input $\mathrm{u}(\mathrm{t})$, then it must be the case that $\theta = \theta^*$.

Definition 2. Locally at-a-point identifiable: At the fixed point θ^* in the parameter space Θ, the system is said to be locally at-a-point identifiable. If for any admissible input $u(t)$ and any parameter vectors θ within an open neighborhood of θ^*, $y(u,\theta) = y(u,\theta^*)$ implies $\theta = \theta^*$.

Identifiability analysis techniques grounded on sensitivities frequently furnish insights into the identifiability within distinct values in the parameter space. Particularly, we assume that the outputs of a model is $y(t_k, \Theta)$ at time t_k with $t_1 \leq t_2 \leq \ldots \leq t_N$ and the parameter vector of Θ. The sensitivity coefficient at each time point $t_k (k = 1, 2, \ldots, N)$ for a given nominal parameter vector is defined as the partial derivative of the system response with respect to a specific parameter, i.e.,

$$\mathrm{s^i_{kj}} = \frac{\partial \mathrm{y_i(t_k, \Theta)}}{\partial \theta_\mathrm{j}}, \tag{7}$$

where y_i $(i = 1, 2, \ldots, d)$ represents the i^{th} element of outputs y $(y \in \mathbb{R}^d)$ and θ_j $(\mathrm{j} = 1, 2, \ldots, \mathrm{q})$ denotes the j^{th} constituent of parameters Θ $(\theta \in \mathbb{R}^q)$. Then, for each observable variable y_i, the sensitivity matrix is considered for all time points by assembling the sensitivity coefficients at every time point into a matrix and it is defined by:

$$\mathrm{S^i_{N\times q}} = \begin{bmatrix} \mathrm{s^i_{11}} & \cdots & \mathrm{s^i_{1q}} \\ \vdots & \ddots & \vdots \\ \mathrm{s^i_{N1}} & \cdots & \mathrm{s^i_{Nq}} \end{bmatrix} \forall \mathrm{i} = 1, \ldots, \mathrm{d}. \tag{8}$$

4.1. **Principal component analysis (PCA) method.** In a real system, a large number of variables and parameters may be involved. However, these variables might not hold equal significance. The aim of principal component analysis (PCA) as proposed is to estimate the decreasing order of importance of the eigenvectors of a symmetric matrix. This means that the most crucial factors are chosen first, followed by the less significant factors [9]. PCA method captures the maximum amount of variability in the data, followed by subsequent components in descending order [10]. The process of PCA involves finding the eigenvalues and eigenvectors of the covariance matrix S formed from the original variables (7). By checking in turn a subset of the eigenvectors corresponding to the smallest eigenvalues, one can effectively compress the dataset without losing significant information. Hence, we need to define the variance of each element of s^i_{kj} by:

$$\mathrm{S^i_c} = \left(\mathrm{s^i_{kj}} - \overline{\mathrm{s^i_{\cdot j}}}\right),$$

where $\overline{s^i_{\cdot j}}$ represents the average of the sum of elements in jth column $s^i_{\cdot j}$ of S^i in (8). Certainly, the covariance matrix of S^i is defined by:

$$\mathrm{Cov}\left(\mathrm{S^i}\right) = \frac{1}{\mathrm{N}} \left(\mathrm{S^i_c}\right)^{\mathrm{T}} \mathrm{S^i_c}.$$

In accordance with the procedural guidelines of the PCA, we arrange the absolute values of the eigenvalues of $Cov\left(S^i\right)$ in ascending order, thereby establishing a sequence that exhibits a continuous increase as below:

$$0 \leq |\lambda^\mathrm{i}_1| \leq \ldots \leq |\lambda^\mathrm{i}_\mathrm{q}| \ \forall \mathrm{i} = 1, \ldots, \mathrm{d}.$$

Let the corresponding eigenvectors are expressed as:

$$\Gamma^\mathrm{i} = (\gamma^\mathrm{i}_1, \gamma^\mathrm{i}_2, \ldots, \gamma^\mathrm{i}_\mathrm{q}) = \begin{bmatrix} \gamma^\mathrm{i}_{11} & \cdots & \gamma^\mathrm{i}_{1\mathrm{q}} \\ \vdots & \ddots & \vdots \\ \gamma^\mathrm{i}_{\mathrm{q}1} & \cdots & \gamma^\mathrm{i}_{\mathrm{qq}} \end{bmatrix} \forall \mathrm{i} = 1, \ldots, \mathrm{d}.$$

Then, we shall delve into the rule of parameter sorting. Commencing with the eigenvector that corresponds to the eigenvalue possessing the most infinitesimal absolute value, we traverse through each component of said eigenvector, seeking out the component with the utmost magnitude, and duly designating the parameter residing at the position of this most eminent

component as unidentifiable. From what has been discussed, we summarize this meticulous process in the following manner:

$$\mathrm{m}_1^{\mathrm{i}} = \arg\left(\max_{1\le \mathrm{j}\le \mathrm{q}} |\gamma_{1\mathrm{j}}^{\mathrm{i}}|\right),$$
$$\mathrm{m}_{\mathrm{l}}^{\mathrm{i}} = \arg\left(\max_{\substack{1\le \mathrm{j}\le \mathrm{q}\\ \mathrm{j}\neq \mathrm{m}_1^{\mathrm{i}},\ldots,\mathrm{m}_{\mathrm{l}-1}^{\mathrm{i}}}} |\gamma_{\mathrm{lj}}^{\mathrm{i}}|\right), \mathrm{l} = 2,\ldots,\mathrm{q}.$$

Additional sorting techniques are elucidated in the scholarly work in [32].

Moreover, we use the residual sum of squares (rss) as a measure of the discrepancies between the actual observations and model predictions by:

$$\mathrm{rss}(\Theta) = \sum_{\mathrm{k}=1}^{\mathrm{N}} [\mathrm{p_k} - \mathrm{y_k}(\Theta)]^2, \tag{9}$$

Using Taylor expansion on (9), we take a linearly approximate function of the rss at Θ^* as:

$$\mathrm{rss}(\Theta^* + \eta\gamma_{\mathrm{j}}) = \mathrm{rss}(\Theta^*) + \eta\gamma_{\mathrm{j}} \cdot \nabla \mathrm{rss}(\Theta^*) + \frac{1}{2}\eta^2 \gamma_{\mathrm{j}}^{\mathrm{T}} \cdot \mathrm{S}^{\mathrm{T}}\mathrm{S} \cdot \gamma_{\mathrm{j}}, \tag{10}$$

where η is described as an arbitrarily small constant, $\nabla rss(\Theta^*)$ is the first derivation of rss with respect to Θ at nominal values and S is defined in (8). If the measurement p_k is exact, then the $\nabla rss(\theta^*)$ will be equal to 0. The second term in (10) is equal to 0 if the observable data are noise-free, i.e.,

$$\mathrm{rss}(\Theta^* + \eta\gamma_{\mathrm{j}}) - \mathrm{rss}(\Theta^*) \approx \frac{1}{2}\eta^2 \gamma_{\mathrm{j}}^{\mathrm{T}} \cdot \mathrm{S}^{\mathrm{T}}\mathrm{S} \cdot \gamma_{\mathrm{j}}.$$

Notice that $S^T S \cdot \gamma_j = \lambda_j \gamma_j$ and $\gamma_j^T \gamma_j = 1$. The rss may change flatter along the direction of the eigenvector γ_j if the eigenvalue λ_j is small enough and the associated parameter is considered as a unidentifiable one in [32].

According to Section 3, we need to identify the remaining parameter vector

$$\Theta = \{\rho, \pi_V, \delta_1, \delta_2, \delta_3, \gamma_I, a, b, c\}$$

with the observable data, so $q = 1,\ldots,9$. We choose the nominal parameter values in column 2 and 3 in Table 2 and utilize the observation time of cumulative cases $\{t_k\}_{k=1,\ldots,53}$ and SARS-CoV-2 loads $\{t_k\}_{k=1,\ldots,21}$ for the PCA method. Note that the multi-scale model comprises 8 state variables and the cumulative cases of C, the outputs can be considered as $d = 1,\ldots,9$. The eigenvalues and their associated eigenvectors of the sensitivity matrix defined in (8) corresponding to known cumulative cases or SARS-CoV loads are given as follows. If the cumulative cases C are known, the eigenvalues of S are calculated by:

$$|\lambda_1^9| = 1.3986 \times 10^{-3},\ |\lambda_2^9| = 9.1924 \times 10^{0},\ |\lambda_3^9| = 1.0353 \times 10^{4},\ |\lambda_4^9| = 3.0246 \times 10^{5},$$
$$|\lambda_5^9| = 1.1637 \times 10^{6},\ |\lambda_6^9| = 1.4644 \times 10^{6},\ |\lambda_7^9| = 7.4070 \times 10^{8},\ |\lambda_8^9| = 7.5634 \times 10^{9},$$
$$|\lambda_9^9| = 1.9692 \times 10^{25},$$

and their associated eigenvectors can be given as:

$$\gamma_1^9 = (1.9785\times10^{-1},\ 5.5616\times10^{-2},\ 1.0043\times10^{-2},\ -8.7710\times10^{-2},\ 1.7328\times10^{-2},\ \mathbf{9.7451\times10^{-1}},\ -4.7050\times10^{-9},\ 5.0363\times10^{-9},\ 2.2466\times10^{-9})^T$$

$$\gamma_2^9 = (-1.2864\times10^{-1},\ -2.2471\times10^{-1},\ -8.8718\times10^{-2},\ \mathbf{9.4353\times10^{-1}},\ -1.3658\times10^{-1},\ 1.2721\times10^{-1},\ 4.0382\times10^{-8},\ -4.3866\times10^{-8},\ -3.4660\times10^{-7})^T$$

$$\gamma_3^9 = (3.3888\times10^{-1},\ \mathbf{7.2760\times10^{-1}},\ -4.4810\times10^{-1},\ 1.3486\times10^{-1},\ -3.9397\times10^{-1},\ -8.6872\times10^{-2},\ 1.7694\times10^{-7},\ 3.6702\times10^{-6},\ -9.8936\times10^{-4})^T$$

$$\gamma_4^9 = (\mathbf{-8.2016\times10^{-1}},\ 8.4242\times10^{-2},\ -5.0415\times10^{-1},\ -1.7553\times10^{-1},\ -1.0871\times10^{-1},\ 1.5303\times10^{-1},\ 1.9829\times10^{-7},\ 1.6624\times10^{-5},\ 5.2188\times10^{-3})^T$$

$$\gamma_5^9 = (-1.0384\times10^{-2},\ 3.8434\times10^{-2},\ 1.8389\times10^{-2},\ 1.5995\times10^{-2},\ 4.5426\times10^{-2},\ 3.5698\times10^{-4},\ -8.8722\times10^{-9},\ -2.3425\times10^{-5},\ \mathbf{9.9788\times10^{-1}})^T$$

$$\gamma_6^9 = (-3.7489\times10^{-1},\ 6.2463\times10^{-1},\ \mathbf{6.1426\times10^{-1}},\ 1.8268\times10^{-1},\ 2.3166\times10^{-1},\ 4.6456\times10^{-2},\ -2.4988\times10^{-7},\ 4.8358\times10^{-4},\ -5.2769\times10^{-2})^T$$

$$\gamma_7^9 = (1.2690\times10^{-1},\ 1.3494\times10^{-1},\ -4.2991\times10^{-1},\ 1.3917\times10^{-1},\ \mathbf{8.6939\times10^{-1}},\ -3.1967\times10^{-2},\ 1.1196\times10^{-7},\ 5.6722\times10^{-2},\ -3.7749\times10^{-2})^T$$

$$\gamma_8^9 = (7.0157\times10^{-3},\ 7.9724\times10^{-3},\ -2.4137\times10^{-2},\ 7.9924\times10^{-3},\ 4.9501\times10^{-2},\ -1.7914\times10^{-3},\ -1.4076\times10^{-8},\ \mathbf{-9.9839\times10^{-1}},\ -2.1936\times10^{-3})^T$$

$$\gamma_9^9 = (-9.1212\times10^{-10},\ -5.3209\times10^{-9},\ -3.7902\times10^{-7},\ -2.7497\times10^{-9},-5.8510\times10^{-8},\ 3.5978\times10^{-10},\ \mathbf{\approx -1},\ 2.0288\times10^{-8},\ 9.9702\times10^{-10})^T.$$

If the SARS-CoV-2 loads V are observable, the eigenvalues of S are

$$|\lambda_1^3| = 1.9871\times10^{-38},\ |\lambda_2^3| = 3.7173\times10^{-36},\ |\lambda_3^3| = 4.4245\times10^{-33},\ |\lambda_4^3| = 2.7687\times10^{-22},$$
$$|\lambda_5^3| = 1.3921\times10^{-21},\ |\lambda_6^3| = 5.9956\times10^{-18},\ |\lambda_7^3| = 4.4947\times10^{-6},\ |\lambda_8^3| = 2.0212\times10^{-1},$$
$$|\lambda_9^3| = 5.0538\times10^{11}.$$

And their associated eigenvectors are as follows:

$$\gamma_1^3 = (-4.1831\times10^{-26},\ 2.1642\times10^{-20},\ \mathbf{-9.9999\times10^{-1}},\ -3.2492\times10^{-3},\ 4.7179\times10^{-5},\ -6.9850\times10^{-13},\ -1.6432\times10^{-19},\ -1.2538\times10^{-24},\ -2.0682\times10^{-15})^T$$

$$\gamma_2^3 = (8.2408\times10^{-24},\ 4.0786\times10^{-20},\ 3.2466\times10^{-3},\ \mathbf{-9.9838\times10^{-1}},\ 5.6804\times10^{-2},\ -4.0945\times10^{-9},\ -7.5797\times10^{-17},\ -3.9854\times10^{-22},\ -2.2066\times10^{-12})^T$$

$$\gamma_3^3 = (-5.5437\times10^{-22},\ 2.3038\times10^{-16},\ -1.3747\times10^{-4},\ 5.6804\times10^{-2},\ \mathbf{9.9839\times10^{-1}}\ 3.9670\times10^{-8},\ 2.9010\times10^{-15},\ 5.2057\times10^{-21},\ 2.2952\times10^{-11})^T$$

$$\gamma_4^3 = (1.9431\times10^{-22},\ -8.1157\times10^{-11},\ 1.8048\times10^{-11},\ -6.3413\times10^{-9},\ -3.9373\times10^{-8},\ \mathbf{\approx 1},\ 1.0510\times10^{-10},\ -7.9626\times10^{-17},\ -7.8220\times10^{-12})^T$$

$$\gamma_5^3 = (-7.6566\times10^{-21},\ 2.2998\times10^{-15},\ -8.2508\times10^{-15},\ 3.5068\times10^{-12},\ 2.2789\times10^{-11},\ -7.8220\times10^{-12},\ 3.3402\times10^{-14},\ 1.7342\times10^{-19},\ \mathbf{\approx -1})^T$$

$$\gamma_6^3 = (3.9981\times10^{-21},\ -2.1094\times10^{-15},\ -3.6355\times10^{-19},\ 1.7973\times10^{-16},\ 2.6545\times10^{-15},$$

$$
\begin{aligned}
&1.0510 \times 10^{-10},\ \approx \mathbf{-1},\ -8.1735 \times 10^{-18},\ -3.3437 \times 10^{-14})^T\\
\gamma_7^3 = (&-8.8818 \times 10^{-16},\ 4.3540 \times 10^{-10},\ -7.3473 \times 10^{-25},\ 6.8369 \times 10^{-22},\ 5.0511 \times 10^{-21},\\
&1.6499 \times 10^{-16},\ 8.1736 \times 10^{-18},\ \approx \mathbf{-1},\ -1.7321 \times 10^{-19})^T\\
\gamma_8^3 = (&1.5233 \times 10^{-6},\ \approx \mathbf{-1},\ -5.3179 \times 10^{-20},\ 1.3046 \times 10^{-17},\ 2.3001 \times 10^{-16},\\
&-8.1157 \times 10^{-17},\ 2.2204 \times 10^{-15},\ -4.3540 \times 10^{-10},\ -2.2998 \times 10^{-15})^T\\
\gamma_9^3 = (&\approx \mathbf{-1},\ -1.5233 \times 10^{-6},\ 6.3783 \times 10^{-26},\ -1.9845 \times 10^{-23},\ -2.0262 \times 10^{-22},\\
&7.0685 \times 10^{-23},\ -7.6379 \times 10^{-22},\ 2.2204 \times 10^{-16},\ 4.1532 \times 10^{-21})^T.
\end{aligned}
$$

If the cumulative COVID-19 cases are known, the largest eigenvalue is λ_9^9 and the largest absolute value of the corresponding element of its associated eigenvector γ_9^9 is approximately 1. In this scenario, the corresponding parameter in the set Θ is identified as a, and a is determined to be the most identifiable parameter. Conversely, if SARS-CoV-2 loads are known, we conduct the PCA method to identify the most identifiable parameter is ρ. After performing the PCA method, the identifiability of the parameter set Θ are ranked from the least identifiable to the most identifiable as follows:

$$\gamma_I,\ \delta_2,\ \pi_V,\ \rho,\ c,\ \delta_1,\ \delta_3,\ b,\ a \text{ for } C,$$

and

$$\delta_1,\ \delta_2,\ \delta_3,\ \gamma_I,\ c,\ a,\ b,\ \pi_V,\ \rho \text{ for } V.$$

4.2. **Eigenvalues method.** The eigenvalues method is one of sensitivity analysis methods to detect the parameter identifiability. Similar to the PCA method, we re-define the sensitive matrix of s_{kj}^i defined in (7) by $s_{(ik)j}$. Then, we reshape the matrix of $s_{(ik)j}$ as below:

$$\mathrm{S} = \begin{bmatrix} \mathrm{s}_{(11)1} & \cdots & \mathrm{s}_{(11)\mathrm{q}} \\ \vdots & \ddots & \vdots \\ \mathrm{s}_{(1\mathrm{N})1} & \cdots & \mathrm{s}_{(1\mathrm{N})\mathrm{q}} \\ \vdots & \vdots & \vdots \\ \mathrm{s}_{(\mathrm{d}1)1} & \cdots & \mathrm{s}_{(\mathrm{d}1)\mathrm{q}} \\ \vdots & \ddots & \vdots \\ \mathrm{s}_{(\mathrm{dN})1} & \cdots & \mathrm{s}_{(\mathrm{dN})\mathrm{q}} \end{bmatrix}. \tag{11}$$

As mentioned earlier, if the two-simultaneous data of cumulative cases and SARS-CoV-2 loads are known, then $d = 2$ in sensitivity matrix of S in (11).

Using the parameter values in column 4 of Table 2, the eigenvalues-eigenvectors of the sensitivity matrix S in (11) for known cumulative cases and SARS-CoV-2 loads are given by:

$$
\begin{aligned}
&|\lambda_1| = 1.6196 \times 10^{-7},\ |\lambda_2| = 3.2552 \times 10^{-5},\ |\lambda_3| = 1.7784 \times 10^{-2},\ |\lambda_4| = 1.7089 \times 10^{0},\\
&|\lambda_5| = 5.8513 \times 10^{4},\ |\lambda_6| = 3.0903 \times 10^{7},\ |\lambda_7| = 1.0306 \times 10^{10},\ |\lambda_8| = 1.1330 \times 10^{15},\\
&|\lambda_9| = 3.9440 \times 10^{25}.
\end{aligned}
$$

$$\gamma_1 = (6.2647 \times 10^{-11},\ -5.4967 \times 10^{-6},\ -5.8927 \times 10^{-7},\ 1.5392 \times 10^{-3},\ -4.4088 \times 10^{-7},\ \mathbf{\approx 1},\ 1.3528 \times 10^{-13},\ -1.0776 \times 10^{-13},\ 3.6848 \times 10^{-5})^T$$

$$\gamma_2 = (7.5412 \times 10^{-10},\ -6.0016 \times 10^{-5},\ 2.6546 \times 10^{-6},\ -5.8168 \times 10^{-3},\ 1.3710 \times 10^{-6},\ 4.5801 \times 10^{-5},\ -6.0271 \times 10^{-13},\ 4.2951 \times 10^{-13},\ \mathbf{-9.9998 \times 10^{-1}})^T$$

$$\gamma_3 = (6.9961 \times 10^{-8},\ 4.3293 \times 10^{-4},\ 1.0557 \times 10^{-3},\ \mathbf{-9.9998 \times 10^{-1}},\ 5.4796 \times 10^{-4},\ 1.5390 \times 10^{-3},\ -2.3743 \times 10^{-10},\ 1.8918 \times 10^{-10},\ 5.8169 \times 10^{-3})^T$$

$$\gamma_4 = (8.6192 \times 10^{-7},\ \mathbf{-9.9998 \times 10^{-1}},\ -6.6453 \times 10^{-3},\ -4.3992 \times 10^{-4},\ -6.1872 \times 10^{-4},\ -4.8260 \times 10^{-6},\ 1.4965 \times 10^{-9},\ -4.9833 \times 10^{-10},\ 6.2556 \times 10^{-})^T$$

$$\gamma_5 = (1.2057 \times 10^{-4},\ -6.6005 \times 10^{-3},\ \mathbf{9.7085 \times 10^{-1}},\ 1.1534 \times 10^{-3},\ 2.3958 \times 10^{-1},\ -1.1337 \times 10^{-6},\ -2.1226 \times 10^{-7},\ 5.5206 \times 10^{-7},\ -3.4072 \times 10^{-6})^T$$

$$\gamma_6 = (-7.6990 \times 10^{-4},\ -9.9123 \times 10^{-4},\ 2.3957 \times 10^{-1},\ -2.7951 \times 10^{-4},\ \mathbf{-9.7088 \times 10^{-1}},\ 1.3788 \times 10^{-7},\ -2.5203 \times 10^{-8},\ 3.1882 \times 10^{-5},\ 9.9032 \times 10^{-7})^T$$

$$\gamma_7 = (4.4642 \times 10^{-5},\ -3.4708 \times 10^{-8},\ 8.1771 \times 10^{-6},\ -8.4764 \times 10^{-9},\ -3.0856 \times 10^{-5},\ 3.9592 \times 10^{-12},\ -6.7849 \times 10^{-10},\ \mathbf{\approx -1},\ 3.0398 \times 10^{-11})^T$$

$$\gamma_8 = (\mathbf{\approx -1},\ -8.9455 \times 10^{-7},\ -6.7397 \times 10^{-5},\ 2.8392 \times 10^{-7},\ 7.7637 \times 10^{-4},\ -7.6655 \times 10^{-11},\ -1.0572 \times 10^{-5},\ -4.4666 \times 10^{-5},\ -1.4665 \times 10^{-9})^T$$

$$\gamma_9 = (1.0572 \times 10^{-5}, -6.1136 \times 10^{-11}, -2.1141 \times 10^{-7}, -3.9940 \times 10^{-12}, -3.4592 \times 10^{-8},\ 6.0426 \times 10^{-16},\ \mathbf{\approx -1},\ 1.1498 \times 10^{-9},\ 2.8950 \times 10^{-14})^T.$$

The remaining eigenvalues and eigenvectors of the matrix S with respect to the matrices C and V are detailed in Appendix A. Following the rank criteria for parameter identifiability outlined in Section 4.1, it is determined that the parameter a is the most identifiable, while the parameter γ_I is the most unidentifiable. The ranking of the identifiable parameters from the least identifiable to the most identifiable is as follows:

$$\gamma_I,\ c,\ \delta_2,\ \pi_V,\ \delta_1,\ \delta_3,\ b,\ \rho,\ a.$$

5. Practical identifiability analysis of multi-scale model

While a parameter may be structurally identifiable under idealized conditions with noise-free data, the presence of noise in real-world data can complicate the identifiability process. To gain a deeper understanding of the model's parameter identifiability, we employ the methodology of Monte Carlo Simulations (MCS) to analyze the practical identifiability of parameters with noisy data. This approach, which is grounded in practicality and randomness, promises to enrich our comprehension of parameter identifiability and guides us toward more robust and informed model analyses. Moreover, this methodology allows for the creation of synthetic datasets that encompass a wide range of potential scenarios, including different noise levels and complexities in the observed data. To initiate the MCS, we shall define a set of fundamental parameters, as specified in the last column of Table 2, and consider them as the actual values in our simulations. Next, we use the MCS method to generate 1000 arrays of fabricated data with various degrees of disturbance based on recorded observations of cumulative cases and SARS-CoV-2 loads. To enrich the analysis and capture the diversity of scenarios, we execute the MCS using two distinct distribution frameworks: Normal and Poisson, which provide a comprehensive exploration of the model's behavior under different statistical profiles. For clarification of the process, we present an outline of the MCS algorithm in Table 3.

TABLE 3. The details of MCS algorithm.

1. Initialization: Set estimated parameters as actual values $\hat{\Theta}$.
2. Data Fabrication: Generate fabricated data using the sampled parameters (Normal distribution sampling or Poisson distribution sampling) and introducing disturbance.
3. Simulated Execution: Run the model using fabricated data for each simulation.
4. Statistical Analysis: Analyze outcomes statistically for simulations with Normal and Poisson distributions and evaluate sensitivity to changes in parameters and disturbance levels.
5. Aggregate Results: Aggregate and compare results across simulations for comprehensive insights about identifiability.

In Table 3, the simulative data for each experiment is generated using the following formulas:

$$\mathrm{Y_1^i} = \mathrm{y_1(x(t_i), \hat{\Theta})} + \zeta_\mathrm{i},\ \mathrm{i} = 1, \ldots, \mathrm{m} \text{ and } \mathrm{Y_2^j} = \mathrm{y_2(x(t_j), \hat{\Theta})} + \zeta_\mathrm{j},\ \mathrm{j} = 1, \ldots, \mathrm{n},$$

where ζ_i and ζ_j represent different levels of measurement errors.

(i) Normal distribution: Random variables Y_1^i and Y_2^j with means of $y_1(x(t_i), \hat{\Theta})$ and $y_2(x(t_j), \hat{\Theta})$, and standard deviations of $y_1(x(t_i), \hat{\Theta})\sigma_0$ and $y_2(x(t_j), \hat{\Theta})\sigma_0$, respectively. That are,

$$\mathrm{Y_1^i} = \mathscr{N}(\mathrm{y_1(x(t_i), \hat{\Theta}), y_1(x(t_i), \hat{\Theta})\sigma_0}) \text{ and } \mathrm{Y_2^j} = \mathscr{N}(\mathrm{y_2(x(t_j), \hat{\Theta}), y_2(x(t_j), \hat{\Theta})\sigma_0}),$$

where $\mathscr{N}(\mu, \sigma)$ denotes a Normal distribution with a mean of μ and a standard deviation of σ. Synthetic data are generated with gradually increasing measurement errors from $\sigma_0 = 0\%$ to $\sigma_0 = 1\%, 5\%, 10\%$ and 20%. In Fig.4, we present visualizations of both cumulative cases and viral load data across various measurement error levels, which true parameters are elements of column 4 in Table 2.

(ii) Poisson distribution: The standard deviation and the mean are defined as follows:

$$\mathrm{Y_1^i} = \mathscr{P}(\mathrm{y_1(x(t_i), \hat{\Theta})}) \text{ and } \mathrm{Y_2^j} = \mathscr{P}(\mathrm{y_2(x(t_j), \hat{\Theta})}),$$

where $\mathscr{P}(\mu)$ represents the poisson distribution with mean μ. Fig.5 depicts the scenarios of the artificial data perturbing by a poisson distribution.

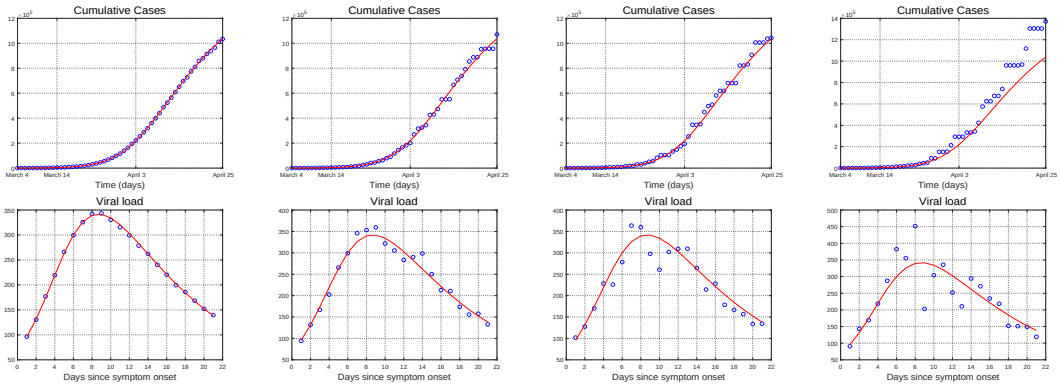


FIGURE 4. The top row of the figure presents a sequence of plots, each displays a single set of cumulative cases generated for the MCS at different measurement error levels. The bottom row in the figure exhibits simulated viral load data. The first column is $\sigma_0 = 1\%$, the second column is $\sigma_0 = 5\%$, the third column is $\sigma_0 = 10\%$, and the fourth column is $\sigma_0 = 20\%$.

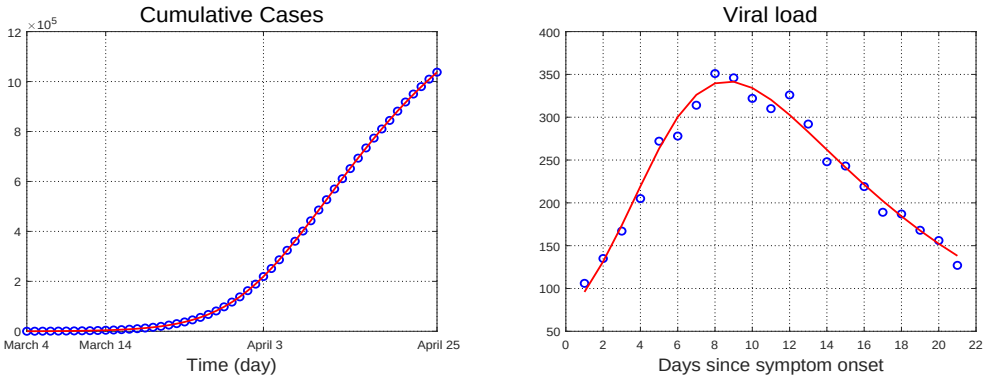


FIGURE 5. The scenarios of cumulative cases and viral load perturbing with a poisson distribution.

Following data generation, the model curve fits each dataset through solving the optimization problems (5) and (6). Subsequently, the Average Relative Errors (AREs) for each parameter are calculated at different noise levels by:

$$\mathrm{ARE}(\theta^{\mathrm{k}}) = 100\% \frac{1}{\mathrm{M}} \sum_{\mathrm{l}=1}^{\mathrm{M}} \frac{|\hat{\theta}^{\mathrm{k}} - \theta_{\mathrm{l}}^{\mathrm{k}}|}{\hat{\theta}^{\mathrm{k}}}, \tag{12}$$

where θ^k is the kth parameter in this set of parameters Θ, $\hat{\Theta}$ represents a true parameter set, where $\hat{\theta}^k$ is the kth parameter in this true set, and Θ_l represents an estimated parameter set, where θ_l^k is the kth parameter in this estimated set.

Applying (12), Tables 4, 5 and 6 provide ARE values corresponding to each parameter and each type of measurement error. Table 7 presents the AREs for all parameters with known cumulative cases and SARS-CoV-2 loads perturbing by a poisson distribution. It's a common observation that the AREs increase as the noise level increases. Thus, a reduction in the amplitude of the AREs as the noise level increases suggests that the associated parameter is unidentifiable. This phenomenon has been observed in Table 4 for parameters ρ, δ_2 and γ_I, and these three parameters are practically unidentifiable. Besides, as the noise level increases up to 20%, c's ARE becomes substantially large, nearly 38 times than 20, and hence c is practically unidentifiable. Conversely, the AREs of other parameters have a negligible change with the increase of the noise, and they are more practically identifiable. Similarly, Table 5 shows that the parameters ρ and π_V are practically identifiable. While the observations from Table 6 indicate that the parameters δ_2, γ_I and c are not identifiable with the cumulative COVID-19 cases and SARS-CoV-2 loads. Absolutely, a notably higher ARE value for parameter b compared to other parameters as the noise is up to 20% that suggests that b is likely unidentifiable with simultaneous dataset. Therefore, the parameters of model (1) and (3) are practically identifiable except parameters δ_2, γ_I, c and b. The outcomes of the MCS method align with the sensitivity-based identifiability analysis discussed in Section 4. As can be seen from Table 7, the parameters of large AREs are consistent regardless of the type of disturbance.

In order to visibly explore the identifiable outcomes, the plots of the rss, which is a function of each parameter of the multi-scale model (1) and (3), are drawn. These plots describe the change of rss in each parameter within a local range while the remaining parameter values are chosen from their actual values in Table 2. These rss plots provide a visual representation of parameter practical identifiability, aiding in understanding of how variations of each parameter influence its identifiability. In the context of rss plots, a somewhat flat plot signifies the potential unidentifiability of the associated parameter within the explored local range.

TABLE 4. The AREs with known cumulative cases (Normal Distribution).

Parameters	$\sigma_0 = 0\%$	$\sigma_0 = 1\%$	$\sigma_0 = 5\%$	$\sigma_0 = 10\%$	$\sigma_0 = 20\%$
ρ	0	91.5	219.3	221.8	212.8
π_V	0	0.7	2.8	6.6	14.3
δ_1	0	0.2	0.6	1.5	3.4
δ_2	0	8.9	11.0	10.6	8.9
δ_3	0	0.6	1.9	2.8	4.7
γ_I	0	7.1	4.2	3.9	3.7
a	0	0.3	0.9	2.1	4.5
b	0	0.2	2.1	6.3	16.2
c	0	28.5	402.1	603.2	757.6

TABLE 5. The AREs with known viral load (Normal Distribution).

Parameters	$\sigma_0 = 0\%$	$\sigma_0 = 1\%$	$\sigma_0 = 5\%$	$\sigma_0 = 10\%$	$\sigma_0 = 20\%$
ρ	0	0.5	2.6	5.4	10.9
π_V	0	0.2	1.2	2.5	5.2
δ_1	0	1.2	1.2	1.5	2.2
δ_2	0	12.5	12.0	12.2	13.9
δ_3	0	2.1	2.6	2.9	3.2
γ_I	0.1	0.7	0.7	0.8	1
a	0	65.6	62.6	67.4	74.5
b	0	16.3	15.8	16.6	18.2
c	0	103.5	121.3	121.5	118.6

TABLE 6. The AREs with known cumulative cases and viral load data (Normal Distribution).

Parameters	$\sigma_0 = 0\%$	$\sigma_0 = 1\%$	$\sigma_0 = 5\%$	$\sigma_0 = 10\%$	$\sigma_0 = 20\%$
ρ	0	0.4	2.0	4.0	8.4
π_V	0	0.2	1.0	2.1	4.1
δ_1	0	0.5	1.3	2.2	3.7
δ_2	0	11.1	11.0	12.9	14.3
δ_3	0	4.6	8.6	9.7	13.3
γ_I	0	4.4	3.9	4.2	4.9
a	0	0.4	1.4	2.9	5.8
b	0	2.3	13.4	29.7	60.7
c	0	63.0	72.6	71.6	57.3

TABLE 7. The AREs of all parameters under Poisson distribution.

Parameters	ρ	π_V	δ_1	δ_2	δ_3	γ_I	a	b	c
Cumulative Cases	7.7	0.2	0.04	3.7	0.1	10.2	0.07	0.009	5.2
Viral Load	2.6	1.3	1.4	10.5	2.6	1.2	68.7	16.0	129.4
Simultaneous	2.4	1.3	0.2	5.3	0.9	14.4	0.2	2.3	60.1

Fig.6 shows that the rss plots of $a, \rho, \pi_V, \delta_1, \delta_3$ reach minimums within the specified range and hence these parameters are practically identifiable. The plots of rss in Fig.7 with parameters b and δ_2 have flat trends and they are unidentifiable. The plots of rss in parameters c and γ_I exhibit repeated fluctuations and so they are practical unidentifiable, which are consistent with the fluctuations in the ARE values of these two parameters in Table 6. Usually, the plot of rss in a model parameter has a minimum point and then associated parameter is considered to be practically identifiable. While a flat trend or an oscillation of the plot of rss in a model parameter means that the corresponding parameter is unidentifiable. In the quest to analyze parameter identifiability, the plots and contour plots of rss in a pair of model parameters are drew in Figs.8, 9 and 10 to highlight the most identifiable and least identifiable parameter combinations with other parameters picked up from their actual values.

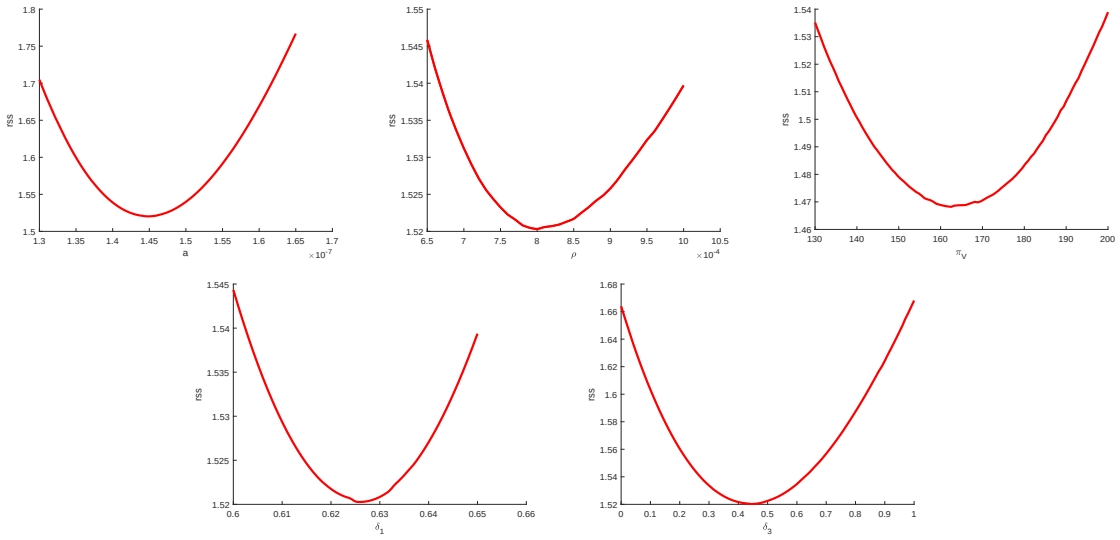


FIGURE 6. rss charts with the most identifiable parameters.

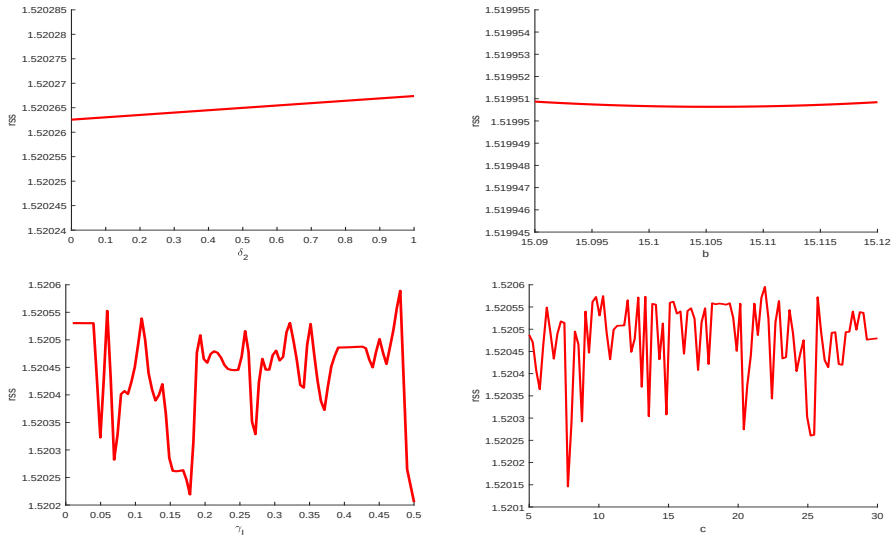


FIGURE 7. rss charts with the least identifiable parameters.

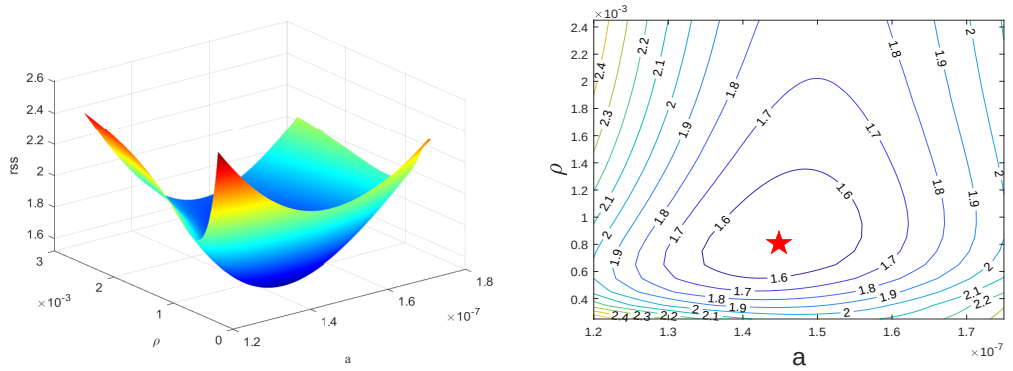


FIGURE 8. The most identifiable parameter combination. Left panel: The surf plot of $a - \rho$. Right panel: The contour map of $a - \rho$.

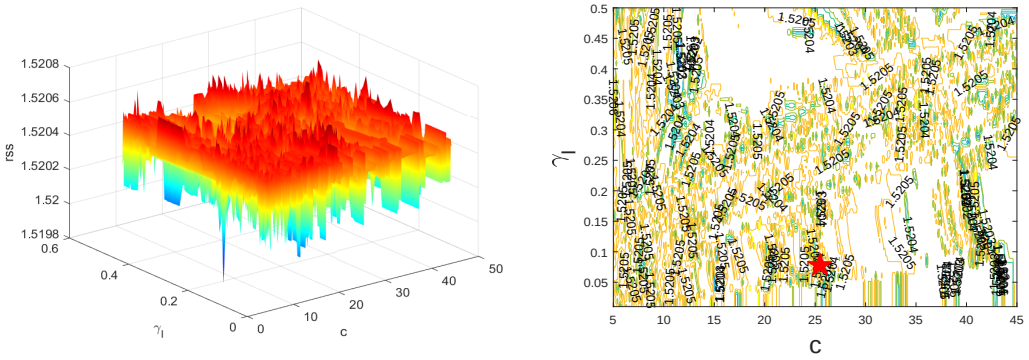


FIGURE 9. The least identifiable parameter combination. Left panel: The surf plot of $c - \gamma_I$. Right panel: The contour map of $c - \gamma_I$.

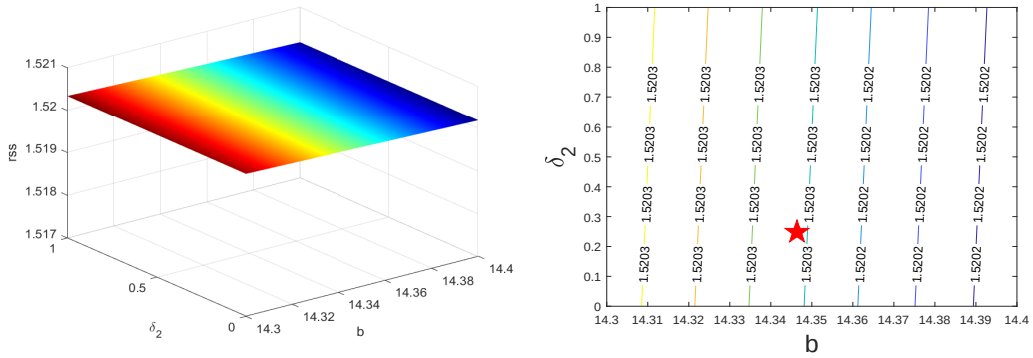


FIGURE 10. The unidentifiable parameter combination. Left panel: The surf plot of $b - \delta_2$. Right panel: The contour map of $b - \delta_2$.

Building upon the findings from the earlier parameter identification research, we have fixed the most identifiable parameters, a and ρ for the purpose of data fitting again. The fitting results are depicted by the solid line in Fig.11. When compared to Fig.3, it is clear that the fitting performance has been improved, with the objective function J decreasing from 1.52 to 1.44. This reduction in the estimation error indicates that the prediction results are now relatively more

accurate. Additionally, this improvement would prompt the implementation of more precise control measures to address the pandemic effectively.

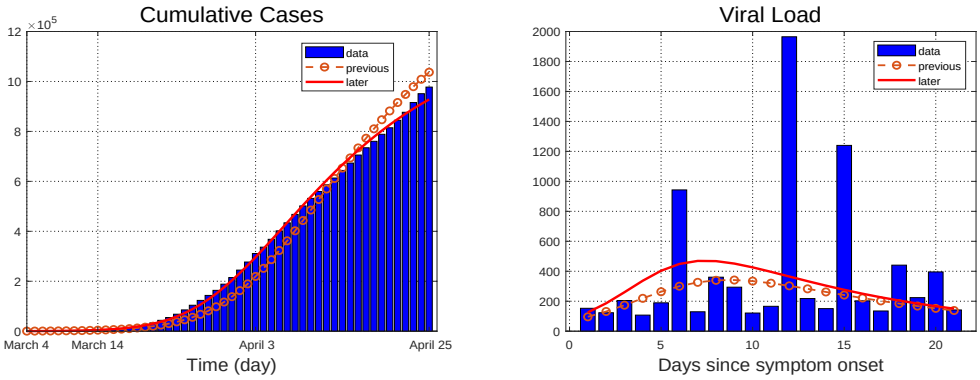


FIGURE 11. The fitting snapshots with both cumulative COVID-19 cases and SARS-CoV-2 loads (blue bars), the red curves relevant the associated solutions to multi-scale model (1) and (3). The dotted line is the previous fit. The solid line is the result of the fit after fixing a and ρ.

6. Approximate Bayesian computation

Previously, we identified the mean values of model parameters by minimizing the objective function (5) and hence, this method always acquires the local optimal solutions. In this section, we make an inference of the identifiability of parameters in the form of their posterior distributions through approximate Bayesian estimation computation [3, 39].

In order to conduct an approximate Bayesian method, we need to first define a prior distribution for each parameter. However, we lack some certain knowledge about the predisposition of their prior distributions, so we prefer to sample the parameter ranges uniformly, which are depicted in the horizontal axis of Fig.12. Consequently, we generate one million parameter vector sets and the vector contains the following parameters

$$\{\rho,\ \pi_V,\ \delta_1,\ \delta_2,\ \delta_3,\ \gamma_I,\ a,\ b,\ c\}. \tag{13}$$

Next, we again use AREs formula (12) to calculate the relative error for each sampled individual parameter set. Finally, we introduce a desired error threshold $\mathcal{R}$, satisfying that if the error of a parameter set is below $\mathcal{R}$, the set is deemed acceptable i.e., the simulation closely matches the experimental data. While the error exceeds $\mathcal{R}$, the parameter set is considered to be rejected. In our model, we set the viral load error threshold to be $\mathcal{R}_V = 0.9805$ and the cumulative cases error threshold to $\mathcal{R}_C = 0.79$. Hence, if the corresponding ARE of parameter set (13) is less than the associated threshold $\mathcal{R}_j (j = V, C)$, then such parameter set is considered to be acceptable.

From the outcomes of the aforementioned framework of the approximate Bayesian computation, we find that there are approximately acceptable 585,700 parameters among the one million sampled parameter sets. Fig.12 visually shows the posterior distributions of the parameters. The diagonal subgraphs of Fig.12 represent the 1-dimensional histogram of the parameters and their peak values giving the best matched parameter values. Each lower triangle subgraph of Fig.12 gives a two-dimensional projection of a two-parameter pair, where red areas denote the high-frequency regions in the posterior distribution. Large area red in Fig.12 states that, given the SARS-CoV-2 load and cumulative COVID-19 cases, we are unable to infer the exact probability distribution of parameters δ_2, γ_I, b, c with their associated upper and lower bounds. These results coincide with the sensitivity-based identifiability of parameters in Section 4.2 and the practical identifiability in Fig.7.

Table 8 lists the aggregate measures, including the mean, median, mode, and standard deviation of the posterior distributions of the estimated parameters with their specific distributions through the approximate Bayesian calculation, which are favored in quantitatively characterizing estimated parameters. In general, if the shape of the posterior probability function of a parameter is narrow and concentrated around a single value, then we say that the parameter is well-identified. While if the shape of the posterior probability function of a parameter experiences widely and dispersedly, we say that the parameter is unidentified. From Table 8, we have noticed that the posterior distributions of parameters $\rho, \pi_V, \delta_1, \delta_3, a$ may obey Gamma, Weibull, and Normal distributions since the prior uniform distributions of those parameters have updated their information after the approximate Bayesian computation. While the parameters δ_2, γ_I, b, c adhere to their prior uniform distributions. Specifically, we find that the mode of γ_I distinctly differs from its mean, suggesting that the acceptable data are not symmetrically distributed around the mean, but they are closely distributed to the mode. Since the Bayesian inference combines prior knowledge and available data to update the probability distribution of model parameters, the final results help in understanding the uncertainty of the estimated parameters and making a relatively accurate prediction.

7. Sensitivity analysis

Sensitivity Analysis (SA) is a valuable tool in epidemiology that allows policy-makers to discern the effects of various parameters on the concerned quantity, offering essential insights for informed decision-making. This method provides useful information on which parameters have the most significant influence on the epidemiological model's prediction. SA empowers policy-makers with valuable insights into the relative importance of different epidemiological parameters, facilitating more effective decision-making in public health strategies. In assessing the severity of SARS-CoV-2 infection, we are concerned with the impact of model parameters on key outcomes, including the basic reproduction number R_0^B.

7.1. **Elasticity analysis.** The elasticity represents the percentage change in quantity Q resulting from a 1% change in parameter θ. Mathematically, the elasticity of quantity Q with respect to parameter θ is formulated by [30]:

$$\gamma_\theta^{\mathrm{Q}} = \frac{\theta}{\mathrm{Q}} \times \frac{\partial \mathrm{Q}}{\partial \theta}. \tag{14}$$

When $\gamma_\theta^Q > 0$, it implies that a 1% increase in θ will cause an γ_θ^Q% increase in Q. When $\gamma_\theta^Q < 0$, it signifies that a 1% increase in θ will lead to an γ_θ^Q% decrease in Q. The index of elasticity analysis is instrumental in making informed decisions and implementing targeted interventions to manage and control the spread of the disease.

We consider the elasticities, $\gamma_\theta^{R_0^B}$, of the basic reproduction number R_0^B. Utilizing (14) and taking other parameters from the column 4 in Table 2, we calculate that

$$\begin{aligned}
&\gamma_{\mathrm{d_{T_I}}}^{\mathrm{R_0^B}} = \gamma_{\mathrm{d_V}}^{\mathrm{R_0^B}} = \gamma_{\mu}^{\mathrm{R_0^B}} = -1,\ \gamma_{\mathrm{a}}^{\mathrm{R_0^B}} = \gamma_{\pi_{\mathrm{V}}}^{\mathrm{R_0^B}} = \gamma_{\mathrm{T}(0)}^{\mathrm{R_0^B}} = \gamma_{\Lambda}^{\mathrm{R_0^B}} = 1,\\
&\gamma_{\alpha}^{\mathrm{R_0^B}} = \gamma_{\mathrm{b}}^{\mathrm{R_0^B}} = -0.8,\ \gamma_{\mathrm{d_T}}^{\mathrm{R_0^B}} = \gamma_{\delta_1}^{\mathrm{R_0^B}} = 0.8,\\
&\gamma_{\epsilon}^{\mathrm{R_0^B}} = \gamma_{\gamma_{\mathrm{A}}}^{\mathrm{R_0^B}} = -0.2,\ \gamma_{\delta_3}^{\mathrm{R_0^B}} = \gamma_{\rho}^{\mathrm{R_0^B}} = 0.2,\\
&\gamma_{\mathrm{c}}^{\mathrm{R_0^B}} = -1.1 \cdot 10^{-4},\ \gamma_{\delta_2}^{\mathrm{R_0^B}} = 1.1 \cdot 10^{-4},\\
&\gamma_{\gamma_{\mathrm{I}}}^{\mathrm{R_0^B}} = 0.
\end{aligned}$$

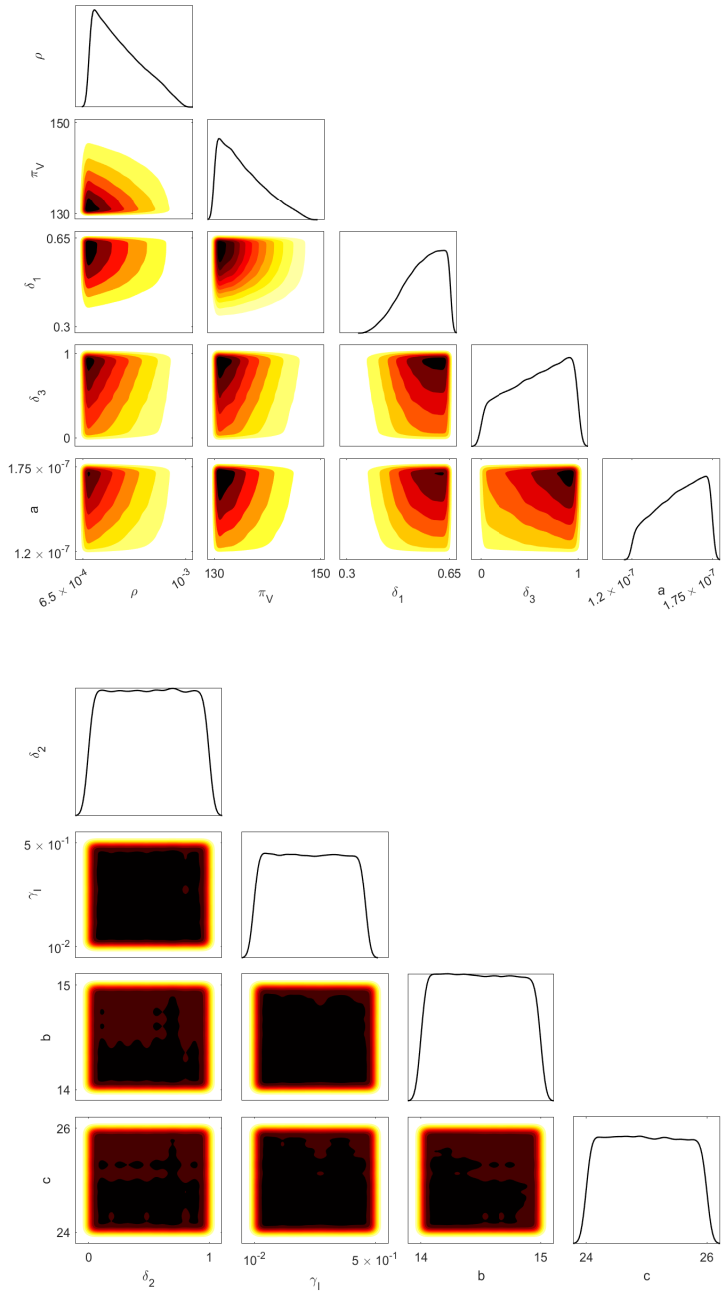


FIGURE 12. Visualizations of acceptable parameters. The diagonal charts serve as 1D histograms of the posterior distribution of each parameter. Below triangle subgraphs gives the 2D projection contour maps, showcasing the frequency of occurrence for pairs of parameters. The darker red color in the contour maps, the more frequent the corresponding parameter values is.

The above results show that certain parameters of model (1) and (3) have almost the same influence on R_0^B. To be specific, the infection rate coefficient a, the virus input rate π_V, the initial count of uninfected epithelial cells $T(0)$, and the natality rate Λ all have the greatest positive influence on R_0^B. On the contrary, it is negatively correlated with the death rate of infected epithelial cells d_{T_I}, the decay rate of SARS-CoV-2 virus d_V, and the natural death rate

μ. These three parameters have the greatest influence on the reduction of R_0^B. By targeting these parameters, public health authorities and policy-makers can effectively reduce the basic reproduction number and control the spread of COVID-19.

TABLE 8. A summation of parameters derived from approximate Bayesian calculations.

Parameters	Mean	Median	Mode	Standard deviation	Posterior distribution
ρ	7.626×10^{-4}	7.469×10^{-4}	6.681×10^{-4}	8.189×10^{-5}	Gamma$(89.6657, 8.5050 \times 10^{-6})$
π_V	135.317	134.502	131.001	3.940	Gamma$(1195.190, 0.113)$
δ_1	0.536	0.546	0.643	0.076	Weibull$(0.568, 8.699)$
δ_2	0.500	0.501	0.675	0.289	Uniform$(0, 1)$
δ_3	0.565	0.593	0.852	0.282	Normal$(0.565, 0.281)$
γ_I	0.2539	0.2535	0.059	0.142	Uniform$(0.01, 0.5)$
a	1.520×10^{-7}	1.537×10^{-7}	1.704×10^{-7}	1.501×10^{-8}	Normal$(1.520 \times 10^{-7}, 1.500 \times 10^{-8})$
b	14.496	14.494	14.223	0.288	Uniform$(14, 15)$
c	24.992	24.988	24.889	0.576	Uniform$(24, 26)$

7.2. **Dynamical sensitivity analysis.** The Latin Hypercube Sampling/Partial Rank Correlation Coefficient (LHS/PRCC) sensitivity analysis is a worthy method for determining key parameters with significant uncertainty in quantities of interest [18, 35]. This technique prioritizes parameters based on the extent to which they contribute to this uncertainty and quantifies the correlation between parameter variations and model outputs. The PRCC analysis aids in prioritizing parameters for further investigation and refinement to minimize uncertainty in the forecasting model. In the context of sensitivity analysis within the LHS/PRCC framework, the most important parameters are typically those with maximal PRCC values. Specifically, parameters that exceed a threshold of 0.2 or fall below -0.2 are considered to have a significant influence on the model outputs and are prioritized for further investigation. These parameters are deemed to contribute significantly to the uncertainty and variability in the forecasted results. Indeed, these PRCC values signify a robust linear relationship between the parameters and the model output, underscoring their fundamental role in comprehending the system's dynamics and behavior. By identifying such strong correlations, we gain insights into the key factors that drive the observed outcomes and can prioritize further surveys and interventions accordingly.

In Fig.13, the time change in the PRCC value for each model parameter is depicted. The graphs illustrate the sensitivities of these parameters to variables V and C at different moments in time, allowing us to observe the dynamic evolution of the parameters within the system. The gray shaded areas signify parameters that have negligible effects on the dynamic process. Their influences on the overall dynamic of the system are considered minor or insignificant. As shown in (a), the parameters ρ and π_V have a significant impact on the variation of viral load. The results match the prior parameter identification findings. As detailed in Section 4 and Table 5, ρ and π_V stand out as the most identifiable for V, i.e. minor adjustments to them result in significant variations in the system output. The viral replication rate, π_V, consistently exerts a positive effect on the viral load throughout the observed time period. This suggests that an increase in the replication rate leads to an increase in the viral load. On the other hand, ρ exhibits more complex behavior. In the first five days, the infection rate has a positive effect on viral load, indicating that a higher infection rate leads to an increasing viral load during this period. However, the effect of ρ subsequently turns negative. Interestingly, around the 9^{th} days, it gradually becomes positive again. After the 100^{th} day, the infection rate becomes the primary factor driving the reproduction of viral load, implying that its influence surpasses that of other factors during this phase. One effective strategy to mitigate viral infection is to prevent the binding between the Spike (S) protein on the surface of the virus and the ACE2 receptor on the host cells. Several approaches have been explored to interfere with the S protein-ACE2 receptor interaction: monoclonal antibodies [42], small molecule inhibitors [24], vaccine and peptide therapeutics [40]. In addition, the RNA-dependent RNA polymerases (RdRp) inhibitors, such

as Remdesivir [14] and Azvudine [51], effectively halt the replication of SARS-CoV-2 virus during reverse transcription.

Similarly, the infection rate ρ in Fig.13 right exhibits complex behavior in relation to cumulative cases. Over the initial thirty days, there is a positive correlation between the increase in ρ and the rise in cumulative cases. Furthermore, a higher scale parameter a and a lower subsaturation coefficient b will amplify the infection rate β between individuals on the spread of the disease. Thus, the rise in the scale parameter a, the infection rate of latent patient δ_1, and asymptomatic patient δ_3 all significantly impact the cumulative cases. This finding aligns with the outcomes of parameter structure identification in Section 4 and practical identification in Table 4. That is, our attention should be on the alterations of parameters a, b, δ_1 and δ_3, as they significantly influence the variability of the prediction results. We suspect that the effect of δ_2 is not significant as the higher infection rate in symptomatic patients necessitates stricter control measures. We can carry out measures such as social distancing [49], wearing masks [4], hand hygiene [23], quarantine, and vaccination coverage to reduce a thereby lowering the probability of transmission. Latent and asymptomatic infections pose significant challenges to epidemic control. To effectively control the outbreak, it is crucial to detect and isolate these individuals promptly. A combined approach of large-scale testing [16] and contact tracing [25] is essential in controlling the spread of COVID-19.

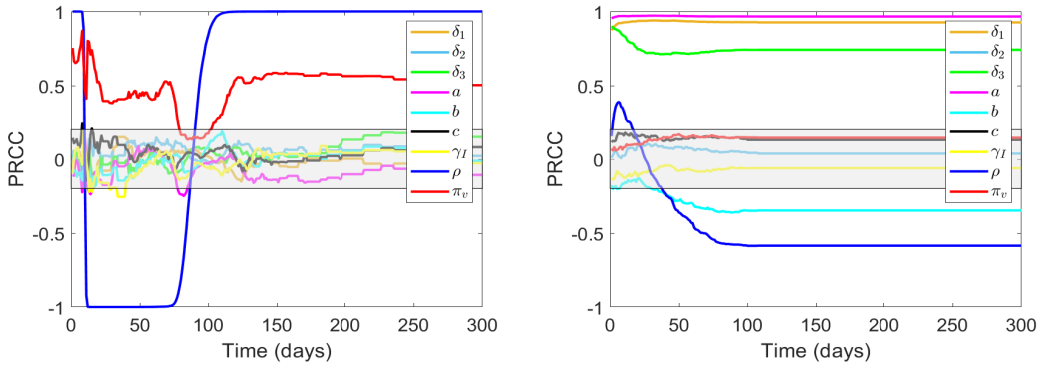


FIGURE 13. The tornado diagrams of the dynamical PRCC values. Left: The tornado diagram of viral load. Right: The tornado diagram of cumulative cases.

8. The influence of treatment, detection and individual heterogeneity

Based on outcomes of parameter identification and sensitivity analysis, we carry out a series of numerical simulations to examine how various factors, such as potential antiviral therapy, technical detection, and individual heterogeneity and behavior, impact the dynamics of infection within individuals as well as the transmission dynamics at the population level. The epidemic prevention and control efforts lasted for three years, so we simulated the progression of the epidemic for 1200 days. Certainly, numerous medications have been utilized for their potential effectiveness in targeting various aspects of COVID-19 pathogenesis [40]. These drugs aim to alleviate symptoms, curtail viral replication, modulate the immune response, or inhibit specific mechanisms that contribute to the advancement of the illness. It is crucial to acknowledge that the effectiveness and safety profiles of these medications are currently being evaluated, and their prescription may be determined by the gravity of the disease and other individual patient considerations. Clinical trials and ongoing research efforts persist in assessing the efficacy of these pharmaceuticals and in investigating potential combination treatment approaches. As is well

understood, antiviral treatments typically have a direct effect on reducing the replication rate π_V of SARS-CoV-2 within a patient. To capture this impact, we substitute π_V with $(1-e_t)\pi_V$, where e_t represents the therapeutic efficiency parameter. Fig.14 shows that antiviral therapy exerts a substantial effect in mitigating the potential risks of COVID-19 at the population level, and there is a considerable reduction in the viral load within an individual due to antiviral therapy. The higher the replication rate of the virus, the more likely it is that the epidemic will persist and potentially recur. Furthermore, an additional strategy for treating viral infections involves blocking the virus from attaching to target cells, thereby hindering its entry and subsequent replication. Fig.15 reveals that a higher value of ρ is associated with a substantial rise in the number of COVID-19 patients, an increased viral load, and an earlier arrival of the peak infection period. And it could be worse than the first wave of the epidemic.

Evidence indicates that the infection rate is positively influenced by the viral load present in an infected individual [22]. Patients with higher levels of SARS-CoV-2 are more likely to expel a greater number of viral particles, increasing the risk of transmission to others. To mimic such an effect, we present a graph depicting the number of COVID-19 cases about the initial viral load. Fig.16 infers that a higher initial viral load can lead to more rapid transmission and potentially more severe symptoms across the population. To effectively contain the spread of COVID-19, close attention must be paid to the initial SARS-CoV-2 load in each patient.

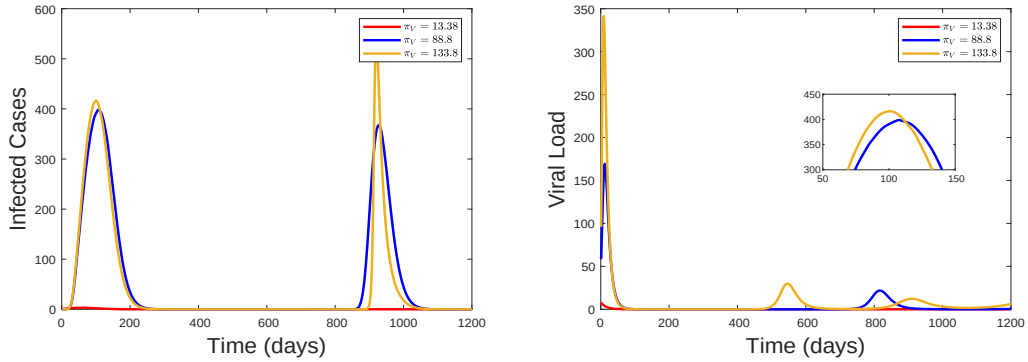


FIGURE 14. Left: The snapshots of COVID-19 cases via π_V. Right: The snapshots of viral load via π_V.

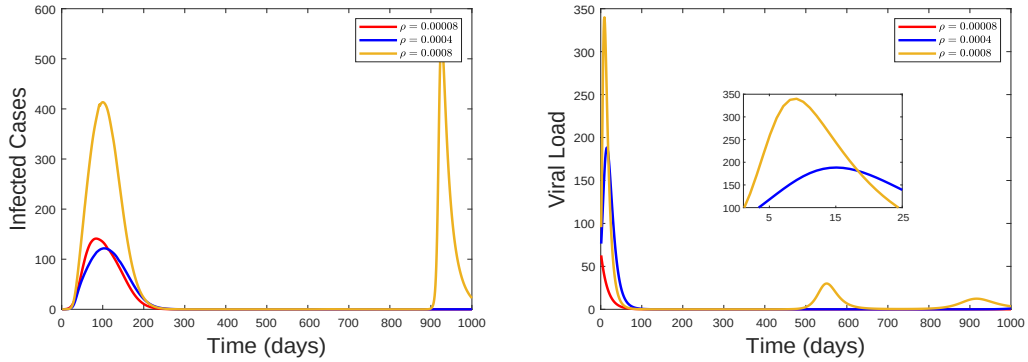


FIGURE 15. Left: The snapshots of COVID-19 cases via ρ. Right: The snapshots of viral load via ρ.

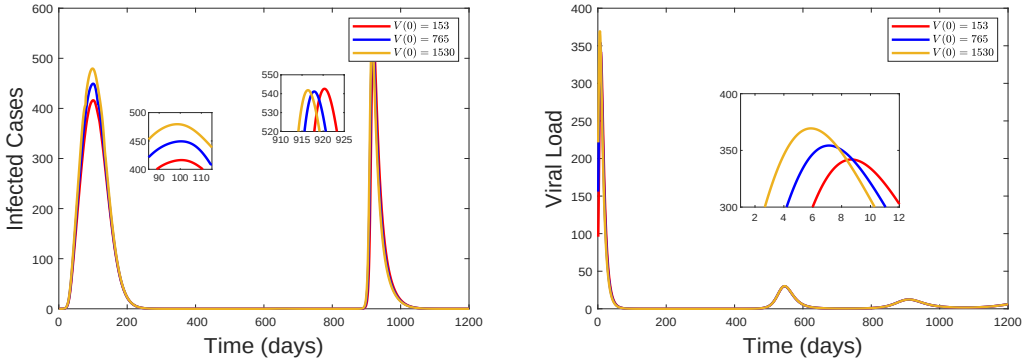


FIGURE 16. Left: The snapshots of COVID-19 cases via $V(0)$. Right:The snapshots of viral load via $V(0)$.

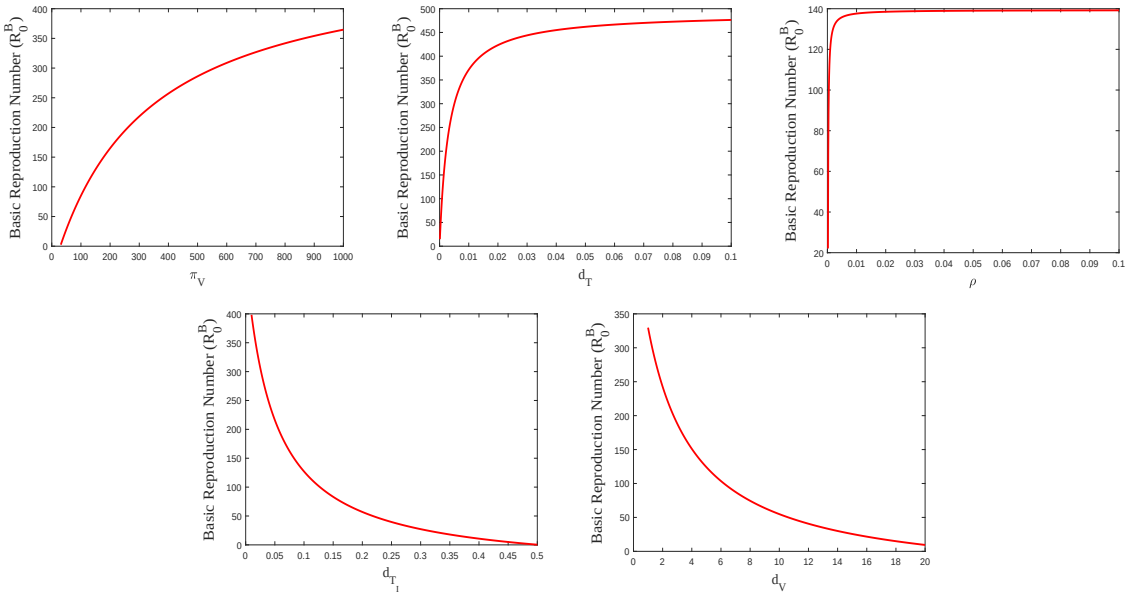


FIGURE 17. Snapshots of R_0^B via parameters of within host model (1).

The basic reproduction number, R_0^B, is a key epidemiological indicator that helps assess the potential for disease transmission and the extent of infection spread. Here, we examine how the model parameters affect the value of R_0^B. Fig.17 reveals that R_0^B increases with the viral replication rate π_V, the death rate of uninfected cells d_T and the infection rate ρ, while it decreases with the mortality of infected cells d_{T_I} and the virus mortality d_V. Higher values of π_V and ρ indicate that each patient contributes more to the viral load within a host, thereby enhancing the potential risk of infection. Consequently, slowing down or inhibiting viral replication and preventing the interaction between viruses and target cells through the administration of antiviral medications [14, 42, 51], vaccines [24], and therapeutic interventions can be effective in reducing the transmission risk and controlling the outbreak of an infection.

9. Conclusion

Parameter identification is a crucial aspect when formulating infectious disease models, constructing reliable analyses, making accurate predictions, and evaluating interventions. If the

parameters in an infectious disease model are unidentifiable, it signifies that the inverse problem is not well-posed, which enables different combinations of parameter values to produce identical predictions. This poses a significant challenge, as it undermines the models predictive power and its ability to inform policy decisions. Particularly, there is an observed disparity of nearly 100,000 patients between the two predicted peaks in Fig.18, despite good fitting results. This discrepancy of the two anticipations may cause different prevention and control measures to be implemented by policy-makers. Hence, it is imperative to invest time and resources into ensuring parameter identifiability to predict and control epidemics effectively.

In this article, we employed sensitivity matrixes to calculate eigenvalues and eigenvectors, thereby providing a clear understanding of the structural identifiability of model parameters with noise-free data. Additionally, we utilized the MCS method to compute the average relative errors (AREs) for ascertaining the practical identifiability of model parameters under various types of stochastic perturbations, including Normal and Poisson noises. Our findings revealed that neither the known cumulative cases nor the viral load data alone could completely identify the model parameter set Θ of the model. This underscores the complexity of infectious disease modeling and the challenges in accurately estimating parameters, especially when dealing with real-world data that is inherently noisy and subject to various sources of uncertainty. Specifically, if we collected cumulative cases, the model parameters would be identifiable except for the infected rate ρ within a patient, the recovery rate γ_I and the death rate c, and the infection rate δ_2 of the symptomatic individual. Conversely, if only the SARS-CoV-2 load were available, the transmission rate ρ within a patient and the release rate π_V would be identifiable. In addition, we demonstrated that when both types of data are known, the unidentifiable parameters of the multi-scale model (1) and (3) include δ_2, γ_I, and c, as well as the half-saturation coefficients b. This emphasizes the importance of having a diverse set of data to ensure the identifiability of a greater number of model parameters.

The least square method and MCS method derive a local result of model parameters when the SARS-CoV-2 load and cumulative cases are known. To overcome such drawbacks, the approximate Bayesian estimation computation approach is based on prior knowledge and the available data to update the posterior distribution of each estimated parameter in a global manner. The identifiable outcomes by the Bayesian estimation computation approach are consistent with those results from the PCA, eigenvalue method, and MCS method. In [19], the authors only examined the identifiability of propagation parameters of a within-host model, focusing exclusively on the analyses of these crucial parameters. Although in [32] has been provided a framework for identifying parameter combinations using differential algebra and implicit function theorem methods, if the model structure becomes complex, direct use of traditional methods may be ineffective when applied to the immuno-COVID-19 model (1) - (3) across two scales. Nevertheless, we have presented a robust and detailed framework for dealing with parameter identifiability of multi-scale models, which can serve as a practical application of the principles underlying differential algebra and implicit function theorem.

Through comprehensive sensitivity analysis in conjunction with parameter identification, we have determined the primary factors that play crucial roles in effectively mitigating COVID-19 transmission, including inhibiting viral replication π_V and infection ρ (as illustrated in Fig.14 and Fig.15), accelerating the death of infected cells d_{T_I} and viruses d_V (as shown in Fig.19 and Fig.20). Special attention must be paid to the initial SARS-CoV-2 loads $V(0)$ and the initial numbers of healthy epithelial cells $T(0)$, as these can significantly impact the spread of COVID-19 at the population level (as depicted in Fig.16 and Fig.21).

This paper acknowledges several limitations. First, we have directly adopted the within-host model (1) from [29] to represent the kinetics of SARS-CoV-2 within a patient and have ignored the interaction between the virus and the immune system response. This interaction plays a crucial role in reducing SARS-CoV-2 infection within the host, and its exclusion from the model might limit our comprehensive understanding of the infection dynamics.

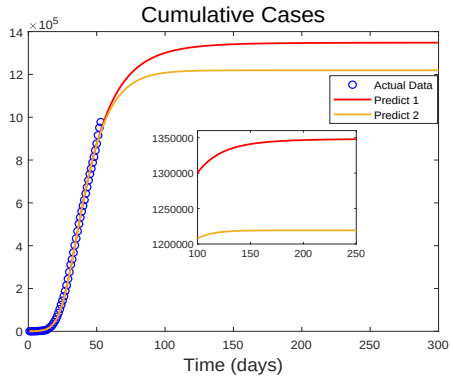


FIGURE 18. The same outputs with two different parameter sets.

Second, the between-host model (3) does not account for the potential transmission route from the entertainment environment to humans, which may underestimate the transmission risk of an infection. Future research should refine these models, incorporate additional factors, and utilize more accurate and reliable data to provide a more comprehensive understanding of SARS-CoV-2 infection and transmission patterns.

10. Acknowledgment

This work was partially supported by Humanities and Social Foundation of Ministry of Education of China (22YJAZH129), the National Natural Science Foundation of China (NNSFC) (Nos. 12271143, 61573016), the Shanxi Province Science Foundation (20210302123454).

References

[1] Adzdzakiy, M.M., Sutarno, S., Asyifa, I.Z., Sativa, A.R., Fiqri, A.RA., Fibriani, A., Ristandi, R.B., et al. SARS-CoV-2 genetic variation and bacterial communities of naso-oropharyngeal samples in middle-aged and elderly COVID-19 patients in West Java, Indonesia, *J. Taibah Univ. Med. Sc.*, Vol.19, No.1, 2024, pp.70-81.

[2] Aguia, M., Dosi, G., Knopoff, D., Virgillito, M. A multi-scale network-based model of contagion dynamics: Heterogeneity, spatial distancing and vaccination, *Math. Models Methods Appl. Sci.*, Vol.31, No.12, 2021, pp.2425-2454.

[3] Anderson, H.G., Takacs, G.P., Harris, D.C., Kuang, Y., Harrison, J.K., Stepien, T.L. Global stability and parameter analysis reinforce therapeutic targets of PD-L1-PD-1 and MDSCs for glioblastoma, *J. Math. Biol.*, Vol.88, No.1, 2024, pp.10.

[4] Anderson, R.M., Heesterbeek, H., Klinkenberg, D., Hollingsworth, T.D. How will country-based mitigation measures influence the course of the COVID-19 epidemic? *Lancet*, Vol.395, No.10228, 2020, pp.931-934.

[5] Bergquist, S., Otten, T., Sarich, N. COVID-19 pandemic in the United States, *Health Policy Technol.*, Vol.9, No.4, 2020, pp.623-638.

[6] Bhapkar, H.R., Mahalle, P.N., Dey, N., Santosh, K.C. Revisited COVID-19 mortality and recovery rates: Are we missing recovery time period? *J. Med. Syst.*, Vol.44, No.12, 2020, pp.202.

[7] Bouchnita, A., Jebrane, A. A hybrid multi-scale model of COVID-19 transmission dynamics to assess the potential of non-pharmaceutical interventions, *Chaos Soliton. Fract.*, Vol.138, 2020, pp.109941.

[8] Chen, B., Zhu, Y., Hu, J., Principe, J.C. Information theoretic parameter estimation, In: Badong C, Yu Z, Jinchun H, Jose C. PrincipeA2 - Badong Chen YZJH, Jose CP, editors, *System Parameter Identification,* Oxford, Elsevier, 2013, pp.29-60.

[9] Chen, H., Zhao, W. *Recursive Identification and Parameter Estimation*, CRC Press, 2014, pp.289-315.

[10] Degenring, D., Froemel, C., Dikta, G., Takors, R. Sensitivity analysis for the reduction of complex metabolism models, *J. Process Control.*, Vol.14, No.7, 2004, pp.729-745.

[11] Delshad, M., Sanaei, M.J., Pourbagheri-Sigaroodi, A., Bashash, D. Host genetic diversity and genetic variations of SARS-CoV-2 in COVID-19 pathogenesis and the effectiveness of vaccination, *Int. Immunopharmacol.*, Vol.111, No.109128, 2022.

[12] Kim, B.N., Abbas, W., Kim, H.K., Yoon, G.J., Kim, H.B., Kim, Y., Kim, S. The importance of proven treatment as a vaccine model for COVID-19, *Appl. Comput. Math.*, Vol.23, No.4, 2024, pp.504-519.
[13] Diekmann, O., Heesterbeek, J.A.P., Roberts, M.G. The construction of next-generation matrices for compartmental epidemic models, *J. R. Soc. Interface.*, Vol.7, No.47, 2010, pp.873-885.
[14] Eastman, R.T., Roth, J.S., Brimacombe, K.R., Simeonov, A., Shen, M., Patnaik, S., Hall, M.D. Remdesivir: A review of its discovery and development leading to emergency use authorization for treatment of COVID-19, *ACS Cent. Sci.*, Vol.6, No.5, 2020, pp.672-683.
[15] Elias, C., Sekri, A., Leblanc, P., Cucherat, M., Vanhems, P. The incubation period of COVID-19: A meta-analysis, *Int. J. Infect. Dis.*, Vol.104, 2021, pp.708-710.
[16] Esbin, M.N., Whitney, O.N., Chong, S., Maurer, A., Darzacq, X., Tjian, R. Overcoming the bottleneck to widespread testing: A rapid review of nucleic acid testing approaches for COVID-19 detection, *RNA*, Vol.26, No.7, 2020, pp.771-783.
[17] Garira, W. A complete categorization of multi-scale models of infectious disease systems, *J. Biol. Dyn.*, Vol.11, No.1, 2017, pp.378-435.
[18] Gomero, B. *Latin Hypercube Sampling and Partial Rank Correlation Coefficient Analysis Applied to an Optimal Control Problem,* Master's Thesis, University of Tennessee, 2012, pp.4-13.
[19] Guillén-González, F., Sevillano-Castellano, E., Suárez, A. Fitting parameters and therapies of ODE tumor models with senescence and immune system, *J. Math. Biol.*, Vol.87, No.5, 2023, pp.67.
[20] Gutierrez, J.B., Galinski, M.R., Cantrell, S., Voit, E.O. From within host dynamics to the epidemiology of infectious disease: Scientific overview and challenges, *Math. Biosci.*, Vol.270, 2015, pp.143-155.
[21] Hassan, M.N., Mahmud, M.S., Nipa, K.F., Kamrujjaman, M. Mathematical modeling and COVID-19 forecast in Texas, USA: A prediction model analysis and the probability of disease outbreak, *Disaster Med. Public Health Prep.*, Vol.17, 2023, pp.e19.
[22] He, X., Lau, E.H.Y., Wu, P., et al. Temporal dynamics in viral shedding and transmissibility of COVID-19, *Nat. Med.*, Vol.26, No.5, 2020, pp.672-675.
[23] Kampf, G. Efficacy of ethanol against viruses in hand disinfection, *J. Hosp. Infect.*, Vol.98, No.4, 2018, pp.331-338.
[24] Kaur, S.P., Gupta, V. COVID-19 vaccine: A comprehensive status report, *Virus Res.*, Vol.288, 2020, pp.198114.
[25] Keeling, M.J., Hollingsworth, T.D., Read, J.M. Efficacy of contact tracing for the containment of the 2019 novel coronavirus (COVID-19), *J. Epidemiol. Commun. H.*, Vol.74, No.10, 2020, pp.861-866.
[26] Khuddush, M., Prasad, K.R. Stability analysis of a fractional order coronavirus (COVID-19) epidemic model, *TWMS J. Appl. Eng. Math.*, Vol.13, No.4, 2023, pp. 1446-1460.
[27] Kou, L., Wang, X., Li, Y., Guo, X., Zhang, H. A multi-scale agent-based model of infectious disease transmission to assess the impact of vaccination and non-pharmaceutical interventions: The COVID-19 case, *J. Safe. Sci. Resil.*, Vol.2, No.4, 2021, pp.199-207.
[28] Ljung, L., Glad, T. On global identifiability for arbitrary model parametrization, *Automatica*, Vol.30, No.2, 1994, pp.265-276.
[29] Li, C., Xu, J., Liu, J., Zhou, Y. The within-host viral kinetics of SARS-CoV-2, *Math. Biosci. Eng.*, Vol.17, No.4, 2020, pp.2053-2861.
[30] Martcheva, M. *An Introduction to Mathematical Epidemiology*, Springer, Berlin/Heidelberg, Germany, Vol.61, 2015, pp.361-382.
[31] Memarbashi, R., Saeedi, S. AN SADR epidemic model with a transport-related infection between two regions, *TWMS J. Appl. Eng. Math.*, Vol.14, No.4, 2024, pp. 1562-1577.
[32] Miao, H., Xia, X., Perelson, A.S., Wu, H. On identifiability of nonlinear ODE models and applications in viral dynamics, *SIAM Rev.*, Vol.53, No.1, 2011, pp.3-39.
[33] Moore, J.P., Offit, P.A. SARS-CoV-2 vaccines and the growing threat of viral variants, *JAMA*, Vol.325, No.9, 2021, pp.821-822.
[34] Pegu, A., O'Connell, S.E., Schmidt, S.D., et al. Durability of mRNA-1273 vaccine-induced antibodies against SARS-CoV-2 variants, *Science*, Vol.373, No.6561, 2021, pp.1372-1377.
[35] Pennington, H.M. Applications of latin hypercube sampling scheme and partial rank correlation coefficient analysis to mathematical models on wound healing, Mahurin Honors College Capstone Experience/Thesis Projects, 2015, pp.32-36.
[36] Prakash, D.B., Vamsi, DKK., Rajesh, D.B., Sanjeevi, C.B. Control intervention strategies for within-host, between-host and their efficacy in the treatment, spread of COVID-19: A multi scale modeling approach, *Comput. Math. Biophys.*, Vol.8, 2020, pp.198-210.
[37] Quaiser, T., Mönnigmann, M. Systematic identifiability testing for unambiguous mechanistic modeling–application to JAK-STAT, MAP kinase, and NF-κ B signaling pathway models, *BMC Syst. Biol.*, Vol.3, No.1, 2009, pp.1-21.

[38] Sakurai, A., Sasaki, T., Kato, S., et al. Natural history of asymptomatic SARS-CoV-2 infection, *N. Engl. J. Med.*, Vol.383, No.9, 2020, pp.885-886.
[39] Saltelli, A., Tarantola, S., Chan, K.P.S. A quantitative model-independent method for global sensitivity analysis of model output, *Technometrics*, Vol.41, No.1, 1999, pp.39-56.
[40] Sanders, J.M., Monogue, M.L., Jodlowski, T.Z., Cutrell, J.B. Pharmacologic treatments for coronavirus disease 2019 (COVID-19): A review, *JAMA*, Vol.323, No.18, 2020, pp.1824-1836.
[41] Skianis, K., Nikolentzos, G., Gallix, B., Thiebaut, R., Exarchakis, G. Predicting COVID-19 positivity and hospitalization with multi-scale graph neural networks, *Sci. Rep.*, Vol.13, No.1, 2021, pp.5235.
[42] Taylor, P.C., Adams, A.C., Hufford, M.M., De La Torre, I., Winthrop, K., Gottlieb, R.L. Neutralizing monoclonal antibodies for treatment of COVID-19, *Nat. Rev. Immunol.*, Vol.21, No.6, 2021, pp.382-393.
[43] Tuncer, N., Marctheva, M., LaBarre, B., Payoute, S. Structural and practical identifiability analysis of Zika epidemiological models, *Bull. Math. Biol.*, Vol.80, 2018, pp.2209-2241.
[44] Tuncer, N., Gulbudak, H., Cannataro, V.L., Martcheva, M. Structural and practical identifiability issues of immuno-epidemiological vector–host models with application to rift valley fever, *Bull. Math. Biol.*, Vol.78, 2016, pp.1796-1827.
[45] Tuncer, N., Timsina, A., Nuno, M., Chowell, G., Martcheva, M. Parameter identifiability and optimal control of an SARS-CoV-2 model early in the pandemic, *J. Biol. Dyn.*, Vol.16, No.1, 2022, pp.412-438.
[46] U.S. Census Bureau, https://www.commerce.gov/data-and-reports/population-statistics.
[47] Van den Driessche, P., Watmough, J. Reproduction numbers and sub-threhold endemic equilibria for compartmental models of disease transmission, *Math. Biosci.*, Vol.180, No.1-2, 2002, pp.29-48.
[48] Wang, X., Wang, S., Wang, J., Rong, L. A multiscale model of COVID-19 dynamics, *Bull. Math. Biol.*, Vol.84, No.9, 2022, pp.99.
[49] Wilder-Smith, A., Freedman, D.O. Isolation, quarantine, social distancing and community containment: Pivotal role for old-style public health measures in the novel coronavirus (2019-nCoV) outbreak, *J. Travel. Med.*, Vol.27, No.2, 2020, pp.1-4.
[50] Yang, Q., Huang, J. Dynamics analysis of an 11-dimensional multi-scale COVID-19 model with interval parameters, *Int. J. Bifurcat. Chaos*, Vol.33, No.12, 2023, pp.2350140.
[51] Yu, B., Chang, J. The first Chinese oral anti-COVID-19 drug Azvudine launched, *Innovation (Camb).*, Vol.3, No.6, 2022, pp.100321.
[52] Zheng, S., Fan, J., Yu, F., et al. Viral load dynamics and disease severity in patients infected with SARS-CoV-2 in Zhejiang province, China, January-March 2020: Retrospective cohort study, *BMJ*, Vol.369, 2020, pp.m1443.

Appendix A. Eigenvalues-eigenvectors for viral load and cumulative cases respectively

If the SARS-CoV-2 load V is known, the eigenvalues of the sensitivity matrix are as below:

$$|\lambda_1^3| = 5.4058 \times 10^{-37},\ |\lambda_2^3| = 4.4041 \times 10^{-33},\ |\lambda_3^3| = 1.1578 \times 10^{-31},\ |\lambda_4^3| = 1.9629 \times 10^{-23},$$
$$|\lambda_5^3| = 9.6736 \times 10^{-23},\ |\lambda_6^3| = 7.6188 \times 10^{-16},\ |\lambda_7^3| = 6.2690 \times 10^{-7},\ |\lambda_8^3| = 5.2919 \times 10^{-1},$$
$$|\lambda_9^3| = 1.8271 \times 10^{10},$$

and the associated eigenvectors are computed by:

$$\gamma_1^3 = (-2.7602 \times 10^{-24},\ 1.6772 \times 10^{-18},\ \boldsymbol{\approx 1},\ -2.6835 \times 10^{-3},\ -2.0052 \times 10^{-5},$$
$$-1.9349 \times 10^{-8},\ -1.8273 \times 10^{-19},\ 2.0095 \times 10^{-23},\ 3.5322 \times 10^{-11})^T$$
$$\gamma_2^3 = (9.5214 \times 10^{-23},\ -1.1861 \times 10^{-17},\ -2.6685 \times 10^{-3},\ \boldsymbol{-9.9515 \times 10^{-1}},\ 9.8322 \times 10^{-2},$$
$$-9.7542 \times 10^{-7},\ -1.3460 \times 10^{-16},\ -2.0157 \times 10^{-21},\ 2.8932 \times 10^{-9})^T$$
$$\gamma_3^3 = (-9.7914 \times 10^{-22},\ 1.2204 \times 10^{-16},\ -2.8380 \times 10^{-4},\ -9.8321 \times 10^{-2},\ \boldsymbol{-9.9515 \times 10^{-1}},$$
$$1.0003 \times 10^{-5},\ 8.9844 \times 10^{-16},\ 2.7386 \times 10^{-20},\ -2.9594 \times 10^{-8})^T$$
$$\gamma_4^3 = (1.1405 \times 10^{-23},\ -8.8214 \times 10^{-19},\ 1.9585 \times 10^{-8},\ 1.2789 \times 10^{-8},\ 1.0051 \times 10^{-5},$$
$$\boldsymbol{\approx 1},\ 7.0139 \times 10^{-13},\ 7.2245 \times 10^{-17},\ 2.1047 \times 10^{-10})^T$$
$$\gamma_5^3 = (-2.3985 \times 10^{-19},\ 3.0840 \times 10^{-14},\ -3.6000 \times 10^{-11},\ -3.0464 \times 10^{-11},\ -2.9735 \times 10^{-8},$$

$$-2.1017\times10^{-10},\ -1.8764\times10^{-14},\ 7.0267\times10^{-19},\ \approx \mathbf{1})^T$$

$$\gamma_6^3 = (-1.4112\times10^{-20},\ 1.5546\times10^{-15},\ 1.5216\times10^{-19},\ -4.9713\times10^{-18},\ 1.0449\times10^{-15},$$
$$-7.0139\times10^{-13},\ \approx \mathbf{1},\ 8.1142\times10^{-15},\ 1.8754\times10^{-14})^T$$

$$\gamma_7^3 = (5.5511\times10^{-16},\ -4.4501\times10^{-11},\ 1.5881\times10^{-23},\ 1.1337\times10^{-23},\ -2.0905\times10^{-20},$$
$$-2.1948\times10^{-16},\ 8.1142\times10^{-15},\ \approx \mathbf{-1},\ 7.8201\times10^{-19})^T$$

$$\gamma_8^3 = (-8.8389\times10^{-6},\ \approx \mathbf{1},\ -1.6742\times10^{-18},\ 1.9933\times10^{-19},\ 1.2261\times10^{-16},$$
$$8.8091\times10^{-19},\ -1.5543\times10^{-15},\ -4.4501\times10^{-11},\ -3.0840\times10^{-14})^T$$

$$\gamma_9^3 = (\approx \mathbf{-1},\ -8.8389\times10^{-6},\ 1.2062\times10^{-23},\ -2.3590\times10^{-25},\ -9.9998\times10^{-23},$$
$$3.6090\times10^{-24},\ 2.8335\times10^{-29},\ 1.1102\times10^{-16},\ 3.2742\times10^{-20})^T.$$

If the cumulative cases C is observable, the eigenvalues of the sensitivity matrix are calculated by:

$$|\lambda_1^9| = 1.4132\times10^{-8},\ |\lambda_2^9| = 3.1879\times10^{-5},\ |\lambda_3^9| = 3.0740\times10^{-3},\ |\lambda_4^9| = 2.6021\times10^{-2},$$
$$|\lambda_5^9| = 5.8247\times10^{4},\ |\lambda_6^9| = 3.0892\times10^{7},\ |\lambda_7^9| = 4.7282\times10^{8},\ |\lambda_8^9| = 1.1330\times10^{15},$$
$$|\lambda_9^9| = 3.9440\times10^{25},$$

and their corresponding eigenvectors are derived such that:

$$\gamma_1^9 = (2.0703\times10^{-10},\ -1.9076\times10^{-4},\ -1.9949\times10^{-6},\ 1.6537\times10^{-3},\ -6.3224\times10^{-7},$$
$$\approx \mathbf{1},\ 4.5147\times10^{-13},\ 3.2125\times10^{-12},\ 3.7691\times10^{-5})^T$$

$$\gamma_2^9 = (5.5547\times10^{-10},\ 1.9804\times10^{-4},\ 4.6401\times10^{-6},\ -5.9940\times10^{-3},\ 1.6495\times10^{-6},$$
$$4.7640\times10^{-5},\ -1.0493\times10^{-12},\ -7.4299\times10^{-12},\ \mathbf{-9.9998\cdot10^{-1}})^T$$

$$\gamma_3^9 = (6.1400\times10^{-7},\ \mathbf{-7.9817\times10^{-1}},\ -6.1733\times10^{-3},\ 6.0239\times10^{-1},\ -8.8489\times10^{-4},$$
$$-1.1483\times10^{-3},\ 1.3886\times10^{-9},\ 1.0155\times10^{-8},\ -3.7689\times10^{-3})^T$$

$$\gamma_4^9 = (-5.5195\times10^{-7},\ 6.0240\times10^{-1},\ 3.3369\times10^{-3},\ \mathbf{7.9818\times10^{-1}},\ -1.9168\times10^{-5},$$
$$-1.2048\times10^{-3},\ -7.5065\times10^{-10},\ -5.2273\times10^{-9},\ -4.6651\times10^{-3})^T$$

$$\gamma_5^9 = (-1.2062\times10^{-4},\ 6.9020\times10^{-3},\ \mathbf{-9.7084\times10^{-1}},\ -1.1560\times10^{-3},\ -2.3963\times10^{-1},$$
$$1.1400\times10^{-6},\ 2.1226\times10^{-7},\ 1.0278\times10^{-5},\ 3.3962\times10^{-6})^T$$

$$\gamma_6^9 = (7.6988\times10^{-4},\ 9.8796\times10^{-4},\ -2.3963\times10^{-1},\ 2.7948\times10^{-4},\ \mathbf{9.7086\times10^{-1}},$$
$$-1.3789\times10^{-7},\ 2.5216\times10^{-8},\ 7.4431\times10^{-4},\ -9.9000\times10^{-7})^T$$

$$\gamma_7^9 = (4.5239\times10^{-5},\ 7.9508\times10^{-7},\ -1.8833\times10^{-4},\ 1.9807\times10^{-7},\ 7.2013\times10^{-4},$$
$$-9.3066\times10^{-11},\ -6.5661\times10^{-10},\ \approx \mathbf{-1},\ -7.0836\times10^{-10})^T$$

$$\gamma_8^9 = (\approx \mathbf{-1},\ -8.9442\times10^{-7},\ -6.7398\times10^{-5},\ 2.8392\times10^{-7},\ 7.7638\times10^{-4},$$
$$-7.6656\times10^{-11},\ -1.0572\times10^{-5},\ -4.4668\times10^{-5},\ -1.4665\times10^{-9})^T$$

$$\gamma_9^9 = (1.0572\times10^{-5},\ -6.1136\times10^{-11},\ -2.1141\times10^{-7},\ -3.9940\times10^{-12},\ -3.4592\times10^{-8},$$
$$6.0426\times10^{-16},\ \approx \mathbf{-1},\ 1.1498\times10^{-9},\ 2.8950\times10^{-14})^T.$$

Appendix B. The influence of within host parameters on COVID-19 infection

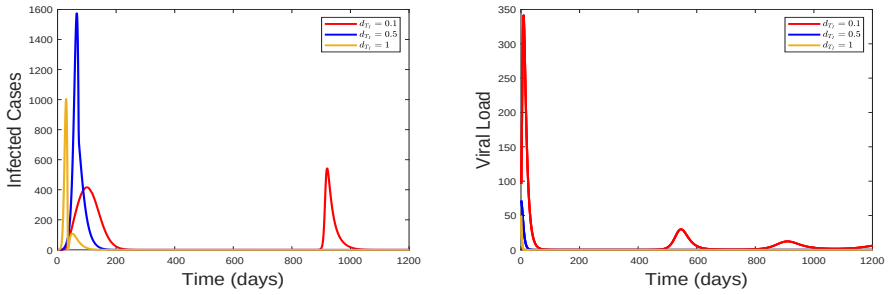


Figure 19. Left: The snapshots of COVID-19 cases via d_{T_I}. Right: The snapshots of viral load via d_{T_I}.

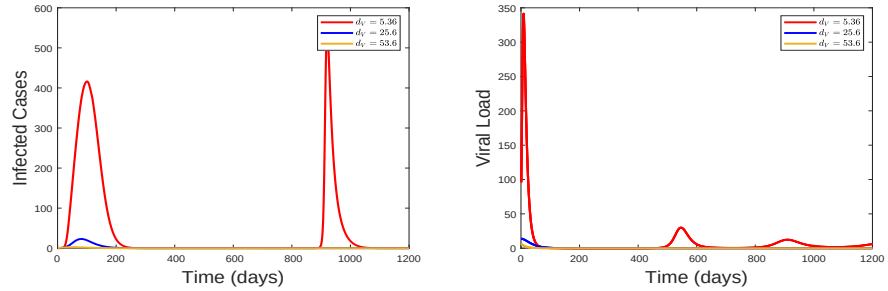


Figure 20. Left: The snapshots of COVID-19 cases via d_V. Right: The snapshots of viral load via d_V.

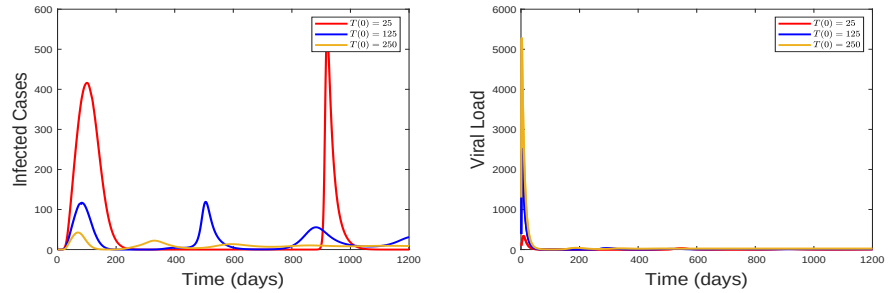
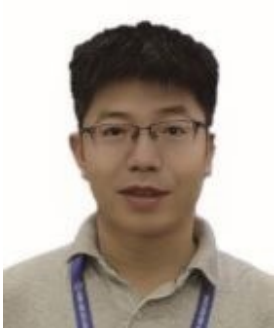


Figure 21. Left: The snapshots of COVID-19 cases via $T(0)$. Right: The snapshots of viral load via $T(0)$.



Junyuan Yang - received his Ph.D. degree in System Engineering from Beijing Institute of Information and Control, China, in 2011. He made his postdoctoral in Wilfrid Laurier University, Canada, during 2012-2013. He is currently working in Complex Systems Research Center at Shanxi University, Taiyuan, China. His main research interest are mathematical biology, complex networks and game theory.



Sijin Wu - received her B.Sc. degree in Mathematics from the School of Mathematics and Statistics, Shanxi Datong University, Datong, China, in 2021. She is currently pursuing a M.Sc. degree in the School of Mathematics and Statistics at Shanxi University, Taiyuan, China. Her main research interest is mathematical biology.



Genhu Di - received his M.Sc. degree in Mathematics from the School of Mathematics and Statistics, Northwestern Polytechnical University, Xi'an, China, in 2011. He is now working in School of Mathematics and Information Technology at Yuncheng University. His main research interest is stochastic dynamics.



Zhen Jin - received his Ph.D. degree in Science from the School of Science, Xi'an Jiaotong University, Xi'an, China, in 2001. He is currently working in Complex Systems Research Center at Shanxi University, Taiyuan, China. His main research interest are mathematical biology and complex networks.